

Influence of upstream disturbances on the primary and secondary instabilities in a supersonic separated flow over a backward-facing step

Hu, Weibo; Hickel, Stefan; Van Oudheusden, Bas

DOI

[10.1063/5.0005431](https://doi.org/10.1063/5.0005431)

Publication date

2020

Document Version

Final published version

Published in

Physics of Fluids

Citation (APA)

Hu, W., Hickel, S., & Van Oudheusden, B. (2020). Influence of upstream disturbances on the primary and secondary instabilities in a supersonic separated flow over a backward-facing step. *Physics of Fluids*, 32(5), Article A15. <https://doi.org/10.1063/5.0005431>

Important note

To cite this publication, please use the final published version (if applicable). Please check the document version above.

Copyright

Other than for strictly personal use, it is not permitted to download, forward or distribute the text or part of it, without the consent of the author(s) and/or copyright holder(s), unless the work is under an open content license such as Creative Commons.

Takedown policy

Please contact us and provide details if you believe this document breaches copyrights. We will remove access to the work immediately and investigate your claim.

Green Open Access added to TU Delft Institutional Repository

'You share, we take care!' - Taverne project

<https://www.openaccess.nl/en/you-share-we-take-care>

Otherwise as indicated in the copyright section: the publisher is the copyright holder of this work and the author uses the Dutch legislation to make this work public.

Influence of upstream disturbances on the primary and secondary instabilities in a supersonic separated flow over a backward-facing step

Cite as: Phys. Fluids **32**, 056102 (2020); <https://doi.org/10.1063/5.0005431>

Submitted: 21 February 2020 . Accepted: 11 April 2020 . Published Online: 04 May 2020

Weibo Hu (胡伟波) , Stefan HICKEL , and Bas van Oudheusden 



View Online



Export Citation



CrossMark

ARTICLES YOU MAY BE INTERESTED IN

[Low-frequency unsteadiness of shock-wave/boundary-layer interaction in an isolator with background waves](#)

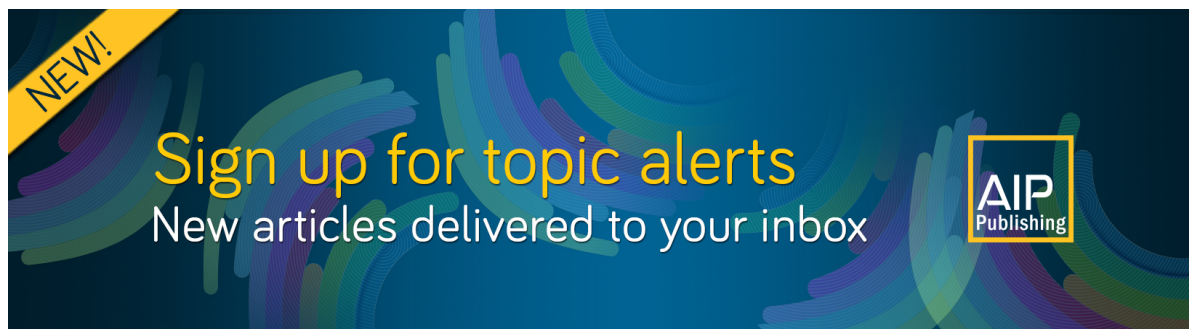
Physics of Fluids **32**, 056105 (2020); <https://doi.org/10.1063/5.0007400>

[Influence of glow discharge on evolution of disturbance in a hypersonic boundary layer: The effect of first mode](#)

Physics of Fluids **32**, 051701 (2020); <https://doi.org/10.1063/5.0008457>

[Unsteady characteristics of compressible reattaching shear layers](#)

Physics of Fluids **32**, 066103 (2020); <https://doi.org/10.1063/5.0008752>



NEW!

Sign up for topic alerts
New articles delivered to your inbox



Influence of upstream disturbances on the primary and secondary instabilities in a supersonic separated flow over a backward-facing step

Cite as: Phys. Fluids 32, 056102 (2020); doi: 10.1063/5.0005431

Submitted: 21 February 2020 • Accepted: 11 April 2020 •

Published Online: 4 May 2020



View Online



Export Citation



CrossMark

Weibo Hu (胡伟波),^{a)}  Stefan Hickel,^{b)}  and Bas van Oudheusden^{c)} 

AFFILIATIONS

Faculty of Aerospace Engineering, Delft University of Technology, Kluyverweg 1, 2629HS Delft, The Netherlands

^{a)} Author to whom correspondence should be addressed: W.Hu-2@tudelft.nl

^{b)} Electronic mail: S.Hickel@tudelft.nl

^{c)} Electronic mail: B.W.vanOudheusden@tudelft.nl

ABSTRACT

The development of primary and secondary instabilities is investigated numerically for a supersonic transitional flow over a backward-facing step at $Ma = 1.7$ and $Re_{\delta_0} = 13\,718$. Oblique Tollmien–Schlichting (T–S) waves with properties according to linear stability theory (LST) are introduced at the domain inlet with zero, low, or high amplitude (cases ZA, LA, and HA). A well-resolved large eddy simulation (LES) is carried out for the three cases to characterize the transition process from laminar to turbulent flow. The results for the HA case show a rapid transition due to the high initial disturbance level such that the non-linear interactions already occur upstream of the step, before the Kelvin–Helmholtz (K–H) instability could get involved. In contrast, cases ZA and LA share a similar transition road map in which transition occurs in the separated shear flow behind the step. Case LA is analyzed in detail based on the results from LST and LES to scrutinize the evolution of T–S, K–H, and secondary instabilities, as well as their interactions. Upstream of the step, the linear growth of the oblique T–S waves is the prevailing instability. Both T–S and K–H modes act as the primary mode within a short distance behind the step and undergo a quasi-linear growth with a weak coupling. Upon pairing of the large K–H vortices, subharmonic waves are produced, and secondary instabilities begin to dominate the transition. Simultaneously, the growth of T–S waves is retarded by the slow resonance between subharmonic K–H and secondary instabilities. The vortex breakdown and reattachment downstream further contribute to the development of the turbulent boundary layer.

Published under license by AIP Publishing. <https://doi.org/10.1063/5.0005431>

I. INTRODUCTION

The backward-facing step (BFS) is one of the canonical geometries in aerospace engineering applications, such as the surface junction of airfoils¹ and engine inlet,² window frame of cockpits,³ and flame holder of combustors.⁴ In the combustor, this geometry can enhance the mixing of fuel and air.⁵ For external flows, the flow field over the BFS has drawn considerable attention for its relevance to triggering laminar-to-turbulent transition at skin joints.^{6,7} Generally, the overall process of boundary layer transition can be divided into three main stages: the receptivity to the external

disturbances, the gradual increase of the initial disturbances by the linear/transient growth of the perturbations or a bypass process, and finally the breakdown to turbulence caused by nonlinear interactions.⁸ However, the specific process of the transition can be very different depending on the configuration or environmental conditions.

For a natural transition, the dominant mechanism is the excitation, amplification, and breakdown of Tollmien–Schlichting (T–S) waves, which are commonly referred to as the first or primary mode in the discrete mode spectrum.⁹ This is the usual transition mechanism encountered on smooth surfaces under quiescent

free-stream conditions. For a subsonic flow, up to $Ma \approx 0.7$, the least-stable T–S waves remain as two-dimensional (spanwise wavenumber equals zero).¹⁰ In the transonic and low supersonic regime, the three-dimensional oblique T–S waves are more unstable than the two-dimensional waves. At much higher Mach numbers, $Ma_\infty \geq 4.0$, other modes become more unstable, which is, however, not our current scope.

Linear stability theory (LST) is widely used to identify these most unstable modes and predict their growth in the early linear stage of the transition process. Reed, Saric, and Arnal⁸ provided a comprehensive overview of the application of LST for boundary layer stability analysis. In the present work, we address a low supersonic flow ($Ma = 1.7$). In this regime, the transition process is initiated by the exponential growth of oblique T–S waves, followed by the occurrence of weakly and strongly nonlinear effects, and finally breakdown to turbulence. In the early linear growth stage, other modes are damped with the development of the transitional boundary layer along the streamwise direction and their interactions with T–S waves can usually be neglected. Mayer, Von Terzi, and Fasel¹¹ further confirmed that the oblique waves can individually induce a fully turbulent boundary layer in supersonic flow, employing LST, parabolized stability equations (PSE), and direct numerical simulation (DNS). The nonlinear process starts with the rapid (transient) growth of the primary modes caused by the interaction of a pair of oblique waves, leading to the generation of streamwise vorticity.¹² Depending on the specific situation, a secondary instability may be induced or a bypass transition occurs. Zhang and Zhou¹³ used PSE to investigate the role of secondary instability in the transition with imposed two-dimensional and oblique T–S waves. Their results showed that the secondary instabilities are not the main mechanism leading to the transition in the flat plate case. The bypass path means that the linear growth of primary or secondary modes is bypassed as a result of forcing disturbances with large amplitude, such as strong free-stream turbulence, pressure gradient, and wall curvature.^{14,15} Abdalla and Yang¹⁶ reported that the Kelvin–Helmholtz (K–H) mode can be the primary instability in the laminar-to-turbulent transition of the laminar separated shear layer without any finite magnitude environmental disturbances. The K–H rolls increase in size and undergo a sinusoidal modulation via the helical instability along the spanwise direction, and the induced highly three-dimensional vortices break down to turbulence with the rolling-up of hairpin vortices.

The backward-facing step is one of the cases where other instabilities than T–S modes may prevail in the transition process.⁶ Overall, there are three main large-scale disturbances observed behind the BFS, including a large primary recirculation eddy as well as Görtler-like and Kelvin–Helmholtz vortices.^{7,17,18} The leading transition mechanism depends on the geometry configuration and is mainly governed by the step height relative to the incoming boundary layer thickness.⁷ When the step height exceeds a critical value, which is a function of unit Reynolds number, the traveling and shedding of the K–H vortices are usually the main driver of the transition process.¹⁷ Furthermore, Eppink *et al.*¹⁹ indicated that transition is accelerated by the interaction of various instability mechanisms behind the step, which can be considered as a modulation of three different types of disturbances with sufficient large amplitudes, but differing in a frequency band. The low-frequency disturbances are

related to traveling waves, while the medium and high frequency contents are associated with T–S waves and shear layer instability, respectively. It seems that the various instabilities and their interactions, instead of the individual effects by the growth of T–S waves, have a great impact on the transition for such a configuration where a separation bubble is present. Simulations by Brinkerhoff and Yaras²⁰ observed that the streamwise vortices induced by the T–S waves are amplified inside the separated shear layer due to the local adverse pressure gradient and develop into coherent hairpin vortices eventually.

In the supersonic regime, the separated shear layer instability has also been widely reported for the BFS case.^{21,22} In our previous work,²³ we have scrutinized the transition path with an unperturbed laminar boundary layer inflow, consisting of the initiation and growth of the K–H vortices, distortion of the large quasi-two-dimensional vortices via the secondary instability, the emergence of the Λ -shaped and hairpin vortices via the vortex breakdown, and finally leading to a turbulent state. Due to the lack of oblique T–S waves in the incoming boundary layer in front of the step, the role of primary T–S modes, their interactions with the excited K–H modes, and the secondary waves in the transition process of the free shear layer, however, are not completely documented and understood. Mayer, Wernz, and Fasel²⁴ numerically investigated the oblique breakdown mechanism of the transition excited by the three-dimensional T–S waves. They first demonstrated that the breakdown to turbulence can be triggered solely by the development of a fundamental primary oblique wave. The interaction between one oblique fundamental wave and two oblique subharmonic waves is also reported. This subharmonic resonance triad can accelerate the laminar-to-turbulent transition. Marxen, Iaccarino, and Shaqfeh²⁵ proposed that the transition is a slow resonant process between the primary and secondary waves in the presence of roughness in which the amplitudes of the excited fundamental and subharmonic secondary waves are augmented significantly. The transient evolution of the primary wave does not usually affect the secondary instability. In addition, the primary waves tend to damp downstream when the excited secondary waves and other large vortices become significant.²⁶ Paredes, Choudhari, and Li²⁷ found that the primary oblique wave can be stabilized by stationary streamwise streaks if the streak spacing is less than half the spanwise wavelength of the primary oblique wave. In contrast, when the streak spacing exceeds this critical value, the primary oblique wave is destabilized by the streaks, which accelerates the oblique breakdown. This nonlinear process usually features staggered Λ -shaped vortices along the boundary layer, the following hairpin vortices caused by lift-up effects, and a breakdown of these coherent vortices via nonlinear interactions between them.²⁸ In the above-mentioned investigations, the primary instability is mainly associated with either T–S or K–H waves solely. In the present work, we investigate how the incoming T–S waves behave in the background of the strong K–H instability and their interactions with the induced secondary instability in the transition process for a $Ma = 1.7$ BFS flow.

This paper is organized as follows: In Sec. II, the numerical setup for the current BFS case is described. Specifically, we present the linear stability theory used to generate the unstable oblique T–S waves that are introduced at the domain inlet as initial boundary conditions. Section III first briefly compares the results for the

investigated three cases with zero, low, and high amplitude perturbations (cases ZA, LA, and HA). Subsequently, a comprehensive analysis is made of the case with low-amplitude oblique waves using both LST and LES. A summary of the main conclusions is given in Sec. IV.

II. FLOW CONFIGURATION AND NUMERICAL SETUP

A. Governing equations

The physical problem is governed by the three-dimensional compressible Navier–Stokes (N–S) equations with adequate boundary and initial conditions, which represent the conservation of mass, momentum, and total energy,

$$\frac{\partial \rho}{\partial t} + \frac{\partial}{\partial x_i}(\rho u_i) = 0, \tag{1}$$

$$\frac{\partial \rho u_j}{\partial t} + \frac{\partial}{\partial x_i}(\rho u_i u_j + \delta_{ij} p - \tau_{ij}) = 0, \tag{2}$$

$$\frac{\partial E}{\partial t} + \frac{\partial}{\partial x_i}(u_i E + u_i p - u_j \tau_{ij} + q_i) = 0, \tag{3}$$

where ρ is the density, p is the pressure, and u_i are the components of the velocity vector.

The total energy E is defined as

$$E = \frac{p}{\gamma - 1} + \frac{1}{2} \rho u_i u_i, \tag{4}$$

the viscous stress tensor τ_{ij} follows the Stokes hypothesis for a Newtonian fluid

$$\tau_{ij} = \mu \left(\frac{\partial u_i}{\partial x_j} + \frac{\partial u_j}{\partial x_i} - \frac{2}{3} \delta_{ij} \frac{\partial u_k}{\partial x_k} \right), \tag{5}$$

and the heat flux q_i is computed by Fourier’s law,

$$q_i = -\kappa \partial T / \partial x_i. \tag{6}$$

The fluid is air and assumed to behave as a perfect gas with a specific heat ratio $\gamma = 1.4$ and a specific gas constant $R = 287.05 \text{ J}(\text{kg K})^{-1}$. Accordingly, the thermodynamic properties follow the ideal-gas equation of state,

$$p = \rho R T. \tag{7}$$

The dynamic viscosity μ and thermal conductivity κ are a function of the static temperature T and are modeled according to Sutherland’s law and the assumption of a constant Prandtl number Pr ,

$$\mu = \mu_{\text{ref}} \frac{T_{\text{ref}} + S}{T + S} \left(\frac{T}{T_{\text{ref}}} \right)^{1.5}, \tag{8}$$

$$\kappa = \frac{\gamma R}{(\gamma - 1) Pr} \mu. \tag{9}$$

The values adopted for the computation are the following: $\mu_{\text{ref}} = 18.21 \times 10^{-6} \text{ Pa s}$, $T_{\text{ref}} = 293.15 \text{ K}$, $S = 110.4$, and $Pr = 0.72$.

B. Flow configuration

The current computational case is an open BFS (i.e., no upper wall) with a supersonic laminar inflow, a schematic of which is shown in Fig. 1. Three cases are considered on the same geometry with different inflow conditions, featuring a laminar zero-pressure gradient boundary layer superimposed with zero-amplitude (case ZA, i.e., clean laminar inflow), low-amplitude (case LA), and high-amplitude (case HA) oblique waves at the inlet.

The laminar inflow is characterized by the free-stream Mach number $Ma_\infty = 1.7$ and the Reynolds number $Re_{\delta_0} = 13718$ based on the inlet boundary layer thickness δ_0 ($99\% u_\infty$) and free-stream values for velocity u_∞ and viscosity μ_∞ . The main flow parameters are summarized in Table I. We indicate free stream flow parameters with subscript ∞ and stagnation parameters with subscript 0. The size of the computational domain corresponds to $[L_x, L_y, L_z] = [110\delta_0, 33\delta_0, 16\delta_0]$ including a length of $40\delta_0$ upstream of the step. The height of the step is three times the inlet boundary layer thickness, which is large enough to trigger the transition from laminar to turbulent flow.¹⁷

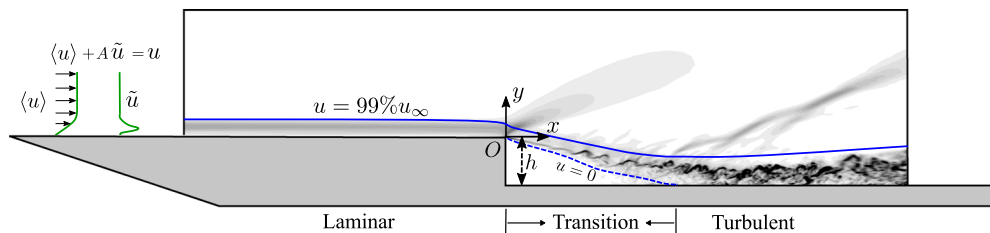


FIG. 1. Schematic of the region of interest, which is in the center of the computational domain with the size of $([-40, 70] \times [-3, 30] \times [-8, 8])\delta_0$ in the x , y , and z directions. This figure represents an instantaneous numerical schlieren graph in the x – y cross section for the low-amplitude perturbed laminar flow case. Indicated are the wall-normal profiles of the mean velocity and perturbations.

TABLE I. Main flow parameters of the current cases.

Ma_∞	u_∞	δ_0	θ_0	Re_∞	T_0	p_0	h	p_∞
1.7	469.85 m/s	1 mm	0.107 mm	$1.3718 \times 10^7 \text{ m}^{-1}$	300 K	$1 \times 10^5 \text{ Pa}$	3 mm	20 259 Pa

C. Numerical method

An implicit large eddy simulation (LES) method of Hickel, Egerer, and Larsson²⁹ is used to solve the governing equations. This technique, the adaptive local deconvolution method (ALDM), provides a spatial discretization scheme with a consistent subgrid scale model for turbulence and shock waves with negligible numerical diffusion in a well resolved laminar flow. An explicit third-order total variation diminishing (TVD) Runge–Kutta scheme is used for time marching.³⁰ This method has been successfully applied to various supersonic flow cases, including shock wave/boundary layer interaction (SWBLI)^{31–33} and laminar to turbulent transition.²³ More details about the numerical method can be found in Refs. 29 and 34.

The numerical grids are generated using a Cartesian structure with block-based local refinement, as displayed in Fig. 2. In addition, hyperbolic grid stretching was used in the wall-normal direction downstream of the step, which is not visible in Fig. 2 due to the high mesh density. The mesh is sufficiently refined near all walls ($y^+ < 1$) to ensure a well-resolved wall shear stress. The grid spacing becomes coarser with increasing wall distance, but the expansion ratio between the adjacent blocks is not larger than two. The distribution of mesh cells is uniform in the spanwise direction. Using this discretization strategy, the computation domain has around 3.6×10^7 grid points; thus, we obtain a spatial resolution of the flow field with $\Delta x_{\max}^+ \times \Delta y_{\max}^+ \times \Delta z_{\max}^+ = 40 \times 0.96 \times 20$ in wall units for the first level grid near the wall in the entire domain ($\Delta x_{\max}^+ = 0.9$ on the step wall). The temporal resolution, that is the time step, is approximately $\Delta t u_{\infty} / \delta_0 = 7.6 \times 10^{-4}$, corresponding to a Courant–Friedrichs–Lewy condition $CFL < 0.5$. The grid convergence of the current setup has been verified in our previous work.²³

The step and wall are modeled as non-slip adiabatic surfaces. All the flow variables are extrapolated at the outlet of the domain. At the inflow and on top of the domain, non-reflecting boundary conditions based on Riemann invariants are used. Periodic boundary conditions are imposed in the spanwise direction. The grid and numerical approach used in the current study are the same for all three cases, except for the inlet boundary conditions. Case ZA has a clean compressible self-similar laminar inflow boundary layer profile, while cases LA and HA contain oblique T–S waves superimposed on the same mean laminar boundary layer profile at the inlet. The setup of the imposed T–S mode will be described in Sec. II D.

D. Oblique wave generation

Linear stability analysis is widely used to study the disturbance growth of a parallel flow in the linear regime with relatively low computational expenses compared with LES and DNS.^{35,36} The spatial variant of LST was employed for the current investigation. According to this approach, the flow variables are decomposed into a steady part \bar{q} and an unsteady perturbation q' , with the latter being represented by harmonic modes,

$$q(x, y, z, t) = \bar{q}(x, y, z) + q'(x, y, z, t) \\ = \bar{q}(x, y, z) + \tilde{q}(y) \cdot e^{i(\alpha x + \beta z - \omega t)} + c.c. \quad (10)$$

The real part of α and β determines the streamwise and spanwise wavenumber, and the imaginary part of α shows the growth rate in the x direction. The angle ϕ of the traveling perturbation waves with respect to the x axis is given by $\arctan(\beta_r / \alpha_r)$. The real and imaginary parts of ω represent the frequency and temporal growth rate, respectively. The term $c.c.$ denotes the complex conjugate of the perturbation in order to obtain a real-valued quantity. In the LST solver, the reference length for these parameters is the local Blasius length $l = \sqrt{\nu_{\infty} x / u_{\infty}}$ ($x / \delta_0 = 382$ at the inlet), for instance, the dimensionless streamwise wavenumber $\alpha^l = \alpha l$. In the following parts, the parameters of wave properties with superscript l are normalized by the Blasius length l , and those with superscript δ are normalized by the inlet boundary layer thickness δ_0 . For the spatial stability analysis, β and ω are prescribed real numbers, while α is the to-be-solved complex number. In this case, the formulation of the perturbations can be rewritten as

$$q'(x, y, z, t) = e^{-\alpha_i x} (\underbrace{\tilde{q}_r \cos \theta - \tilde{q}_i \sin \theta}_{\text{real part}}) + i e^{-\alpha_i x} (\underbrace{\tilde{q}_r \sin \theta + \tilde{q}_i \cos \theta}_{\text{imaginary part}}), \quad (11)$$

where $\theta = \alpha_r x + \beta z - \omega t$. The base flow \bar{q} and perturbations \tilde{q} are substituted into the compressible N–S equations. The linearized N–S equations are then further simplified by the parallel-flow assumption to the Orr–Sommerfeld (O–S) equations. With appropriate boundary conditions, these equations represent an eigenvalue problem. In the spatial analysis, the resulting eigenvalues of the O–S equations are the complex wavenumber α , and the corresponding complex eigenfunctions are the disturbances of the three velocity components, pressure, and temperature. The LST solver used in the

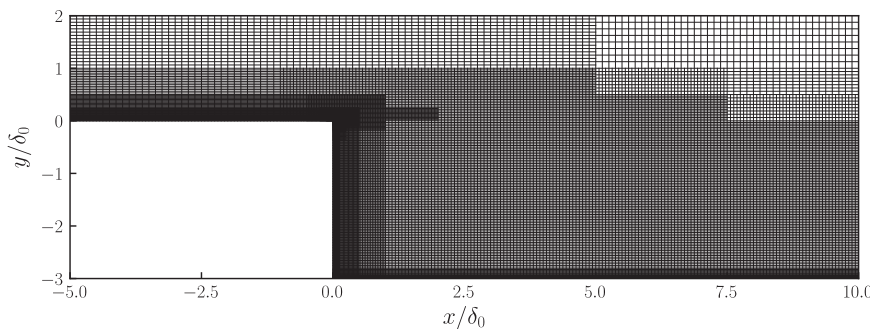


FIG. 2. Details of the numerical grid depicted in the x - y plane in the computational domain near the step. For clarity, every second point in the x direction and fourth point in the y direction are plotted.

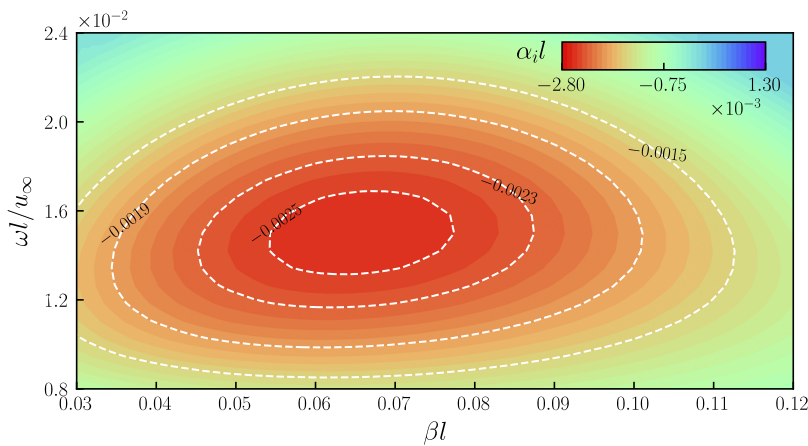


FIG. 3. Contours of α_i at the domain inlet obtained from LST.

present study is a validated in-house code whose numerical details and validation have been reported previously.^{37–39}

For the present BFS case, the compressible base flow was computed by using a selective frequency damping technique.⁴⁰ Next, spatial LST is used to find the local most unstable mode, i.e., corresponding to the smallest negative value of α_i^l , within a range of $0.03 \leq \beta^l \leq 0.12$ and $0.008 \leq \omega^l \leq 0.024$. Figure 3 shows the contours of α_i^l at the local Reynolds number $Re_l = 2167$ based on the Blasius length. As we can see, the maximum $|\alpha_i^l|$ is reached at $\alpha_i^l = -0.00255$ for $\beta^l = 0.06202$ and $\omega^l = 0.01605$. The corresponding streamwise wave number and wave angle are $\alpha_r^l = 0.04001$ and $\phi = 57.17^\circ$, respectively. It has been reported that for the similar flow conditions, the wave angle of the primary mode is between $\phi = 55^\circ \sim 60^\circ$ (at $Ma > 1.6$), the streamwise wave number $\alpha_r^l = 0.035\text{--}0.09$ (at $Re_l = 2000$ and $Ma = 1.6$), and angular frequency $\omega^l = 0.006\text{--}0.03$ (at $Re_l = 2000$ and $Ma = 1.6$).^{12,41,42} Our results fall into this reported range.

The eigenvalues spectra and corresponding disturbance profiles of the most unstable oblique wave are plotted in Fig. 4. The horizontal branch on the left represents the fast acoustic wave spectrum and

the one on the right the slow acoustic wave spectrum [see Fig. 4(a)].⁴³ These two continuous horizontal spectra are generated from the streamwise wavenumber α_r , corresponding to the phase velocities $c_{ph} = 1 \pm 1/Ma$. The vertical branch denotes the continuous vorticity and entropy spectra $c_{ph} = 1$. At the current Reynolds number, these two branches overlap and become indistinguishable, which is a common behavior in high Reynolds number flow, as reported by Balakumar and Malik.⁴⁴ The mode with a minimum negative value belongs to another continuous spectrum (most of them are not shown in the plot due to their large imaginary magnitudes), which will decay rapidly with the streamwise distance and therefore is not our current concern. These spurious modes can be identified by examining their eigenfunctions. The other discrete mode in the fourth quadrant is the T-S mode and has the largest growth rate among all the physical modes. Figure 4(b) shows the perturbation profiles of the velocity components, pressure, and temperature for this mode. We substitute the computed α_r , β , and ω into Eq. (11), retaining only the real part of q' , where $e^{-\alpha_r x}$ is set as a constant initial amplitude. We consider two cases: with low amplitude ($e^{-\alpha_r x} = 0.026$, case LA) and high amplitude ($e^{-\alpha_r x} = 0.26$, case HA). Correspondingly, the averaged amplitude of the streamwise velocity fluctuations is

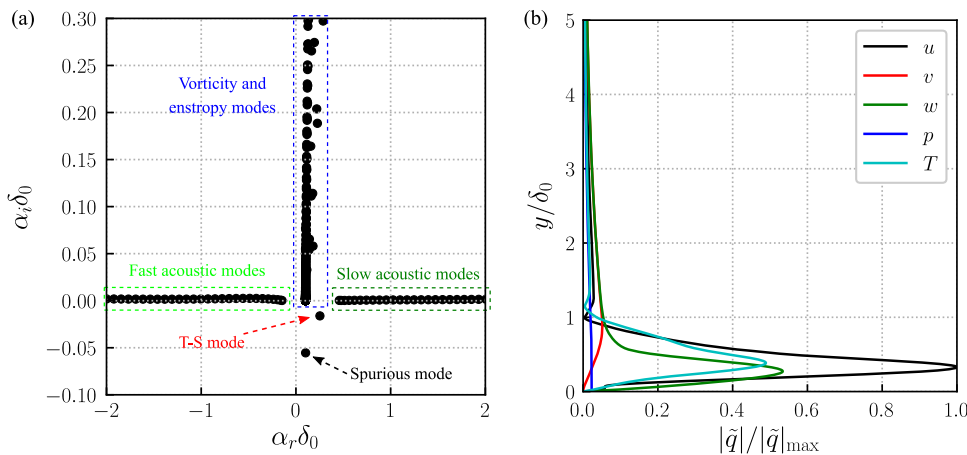


FIG. 4. (a) Eigenvalue spectra and (b) the wall-normal disturbances of the local least stable T-S mode at $\omega \delta_0 / u_\infty = 0.10164$ and $\beta \delta_0 = 0.39270$ obtained from LST.

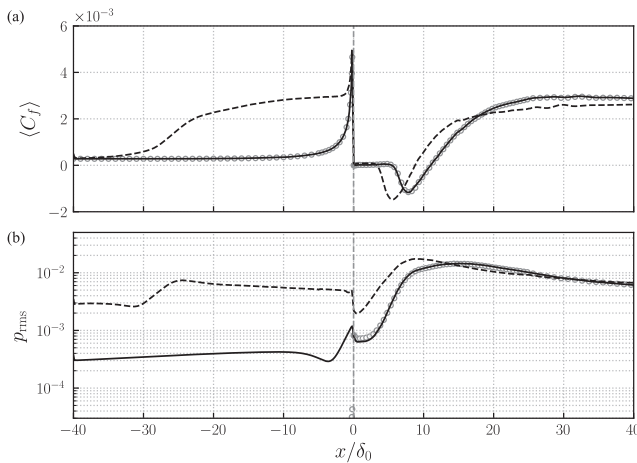


FIG. 5. Streamwise development of the time and spanwise-averaged (a) skin friction and (b) root mean square of wall pressure fluctuations (normalized by $\rho_\infty u_\infty^2$) for case ZA (o), case LA (—), and case HA (----).

equivalent to $A_{in} = 0.1\%u_\infty$ (case LA) and $A_{in} = 1\%u_\infty$ (case HA) in the disturbed region ($0 \leq y/\delta_0 \leq 5.0$).

III. RESULTS

We first compare the transition process of the boundary layer among the three cases ZA, LA, and HA in this section to investigate the impact of the initial disturbance level on the transition process. The main involving instabilities are identified by the visualization of the instantaneous vortical structures. Case LA shows T-S, K-H, and secondary waves most clearly. Our focus then is put on this most interesting case, i.e., the low-amplitude oblique waves case, to discuss the interaction among the oblique T-S, K-H, and secondary modes.

A. Comparison of transition process with different initial disturbance levels

First of all, an overview of the boundary layer development is provided by discussing the streamwise variation of the time- and spanwise-averaged skin friction, as shown in Fig. 5(a). The curves for cases ZA and LA coincide. The boundary layer remains laminar upstream the step, as can be inferred from the low level of $\langle C_f \rangle$. In the first half of the separation bubble ($0.0 \leq x/\delta_0 \leq 5.1$), the recirculating flow is still laminar, and $\langle C_f \rangle$ is approximately zero. Then, $\langle C_f \rangle$ decreases toward a global minimum at $x/\delta_0 \approx 8.0$, followed by an increase in $\langle C_f \rangle$. In both cases, the shear layer reattaches around $x/\delta_0 = 10.9$. For case HA, the transition occurs much faster than for the other two cases. Skin friction begins to grow shortly downstream the inlet at $x/\delta_0 \approx -33.0$, which indicates an early onset of transition. After a quick growth between $-28.0 \leq x/\delta_0 \leq -21.0$, $\langle C_f \rangle$ reaches a typical turbulent level,⁴⁵ indicating that the boundary layer is already quite turbulent upstream the step. As a result of the more energetic shear layer and, thus, the promotion of mixing, the reattachment length ($L_r/\delta_0 = 8.8$) is 19% shorter than for the other two cases. The skin friction coefficient reaches a steady value at about $\langle C_f \rangle = 2.9 \times 10^{-3}$ for all the cases at $x/\delta_0 > 30$. Table II compares the reattachment length L_r from the current LES with existing experimental and numerical results normalized with the step height h . In the laminar case, the obtained $L_r/h = 3.63$ agrees well with the value reported by Karimi, Wijeyakulasuriya, and Nalim⁴⁶ for their low-turbulence case (turbulence intensity $I = 0.5\%$) and is smaller than the one reported by Zhu *et al.*²² due to the lower Ma in the current case. For the turbulent case, it can be seen that $L_r/h = 2.93$ is very close to the reported values, for example, $L_r/h = 3.0$ reported by Chakravarthy, Arora, and Chakraborty.⁴⁷

The root mean square (rms) of the wall pressure $p_{rms} = \sqrt{\overline{(p'p')}}/\rho_\infty u_\infty^2$ is plotted in Fig. 5(b), illustrating the level of fluctuations and the generation of turbulence. Due to the imposed oblique waves, the rms of wall pressure for cases LA and HA is around two and three orders higher than for the clean laminar inflow case at the inlet [not visible in Fig. 5(b)]

TABLE II. Comparison of the reattachment length reported in various studies. Note that the reference length δ_0 is the boundary layer thickness in front of the step in some cases, and I is the free stream or maximum inflow turbulence intensity.

Authors	Ma	Re_∞ (m^{-1})	h (mm)	δ_0/h	L_r/h	Comments
Chakravarthy, Arora, and Chakraborty ⁴⁷	1.5	4.41×10^7	6.35	0.32	3.0	LES, $I \approx 6\%$
Roshko and Thomke ⁴⁸	2.0	3.74×10^7	6.35	0.54	3.36	Experiment, turbulent
Liu <i>et al.</i> ⁴⁹	2.0	3.35×10^7	3.18	0.25	3.0	LES, $I \approx 1\%$
Soni, Arya, and De ¹⁸	2.0	3.34×10^7	3.2	...	4.1	LES, $I \approx 2.9\%$
Karimi, Wijeyakulasuriya, and Nalim ⁴⁶	2.0	3.32×10^7	3.18	...	3.56	Rans, $I \approx 0.5\%$
Bolgar, Scharnowski, and Kähler ⁵⁰	2.0	2.77×10^7	7.5	0.47	3.24	Experiment, $I \approx 2\%$
Chen <i>et al.</i> ⁵¹	3.0	0.77×10^7	5	...	3–4	Experiment, turbulent
Zhu <i>et al.</i> ²²	3.4	0.610×10^7	3	0.33	5.9	Experiment, laminar
Zhu <i>et al.</i> ²²	3.4	0.610×10^7	3	0.33	3.6	Experiment, turbulent
Present case ZA	1.7	1.37×10^7	3	0.33	3.63	LES, laminar
Present case LA	1.7	1.37×10^7	3	0.33	3.63	LES, $I \approx 0.8\%$
Present case HA	1.7	1.37×10^7	3	0.33	2.93	LES, $I \approx 8\%$

due to its level lower than 10^{-5}]. In case HA, the pressure fluctuations start to increase at $x/\delta_0 = -31.0$, which confirms that transition is initiated at this point. After reaching a local maximum at $x/\delta_0 = -24.0$, they gradually reduce to a level of $p_{rms} = 0.005$ upstream the step. For cases ZA and LA, the pressure fluctuations grow very slowly upstream the step. Behind the step, all three cases display a similar variation tendency, but with different rates. Case HA has a higher initial level of the pressure

fluctuations after the step and a higher peak value than the other two cases. Case LA follows nearly the same trajectory as case ZA downstream the step, notwithstanding it being imposed with low-amplitude oblique waves, which provides further support for the assumption that these two cases share the same transition path throughout the separated shear layer region. The wall pressure fluctuations finally reach identical levels for all three cases at $x/\delta_0 > 30$.

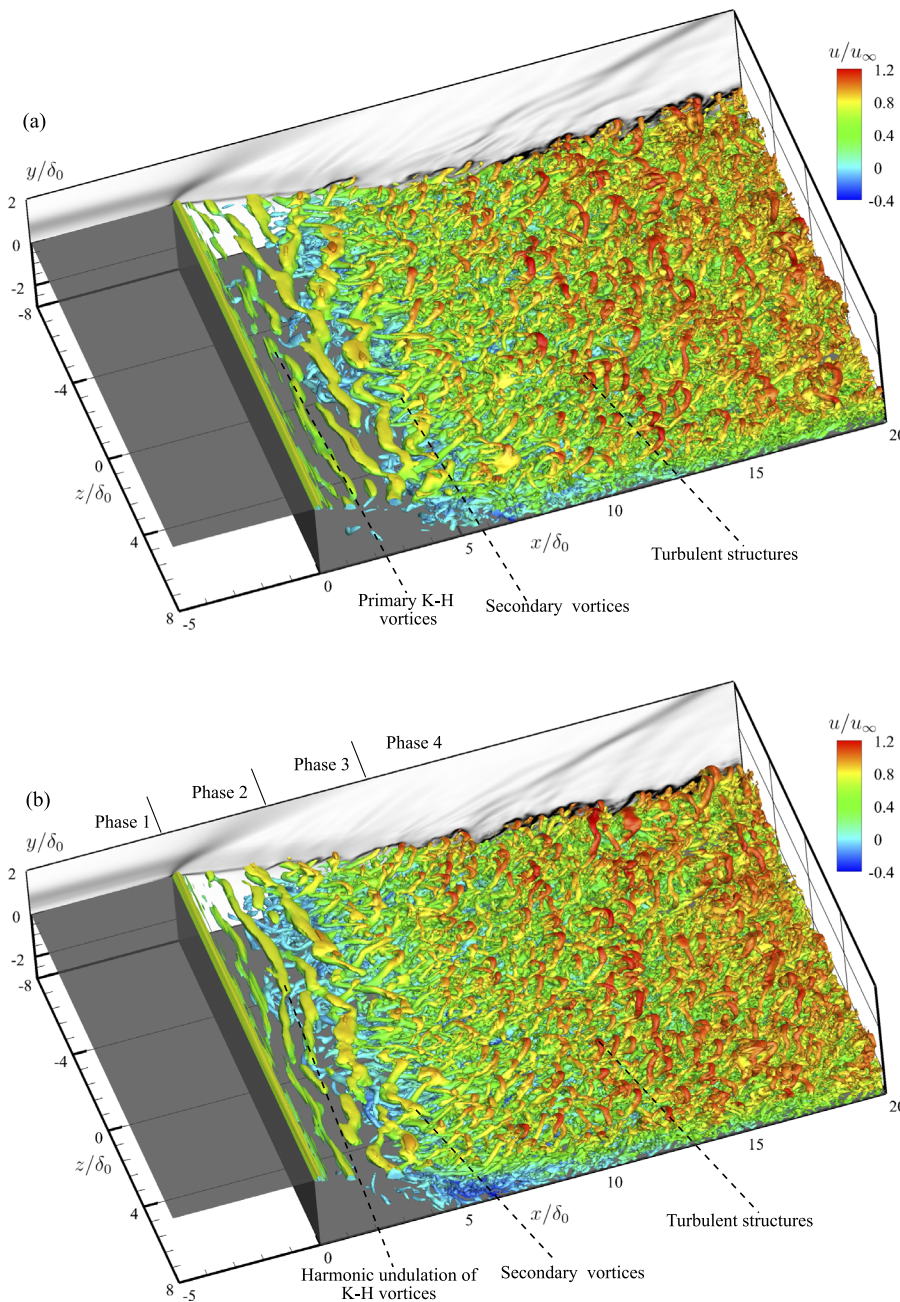


FIG. 6. Instantaneous vortical structures at $tu_\infty/\delta_0 = 912$, visualized by isosurfaces of λ_2 . A numerical schlieren based on the $z = 0$ slice is also included with $|\nabla\rho/\rho_\infty = 0-1.4$. (a) Case ZA and (b) case LA at $\lambda_2 = -0.02$.

The visualization of instantaneous vortical structures for all three cases is presented by means of isosurfaces of the λ_2 vortex criterion⁵² in Figs. 6 and 7. For both cases ZA and LA, there is a strong shear layer produced at separation, which is subject to the inviscid instability, inducing large K–H vortices. Subsequently, these large vortices break down into small vortices as they move toward the bottom wall, which is likely caused by the secondary instability. Finally, a fully turbulent boundary layer flow develops downstream of the separation bubble, as illustrated by the small hairpin vortices resulting from the breakdown of the large Λ -shaped vortices and reattachment of all these unsteady waves. These similar features of the instantaneous flow field provide further confirmation that cases ZA and LA follow the same transition path. For the low-amplitude

case, however, the development of the upstream boundary layer also shows the imposed oblique T–S waves upstream the step, as shown in Fig. 5 and will be discussed in more detail in Sec. III B 1. In contrast, case HA undergoes a much earlier transition, which takes place already in the attached boundary layer upstream of the step [Fig. 7(a)]. The visualization shows oblique vortices that are excited by the large-amplitude T–S waves and their secondary instabilities, which form the arc-shaped vortices. These disturbances of the boundary layer already become highly three-dimensional upstream of the step. Since the incoming flow is effectively turbulent at the step [Fig. 7(b)], the free shear layer of case HA is more unsteady (turbulent) than for case ZA/LA. Note that the increased level of λ_2 in Fig. 7(b) is aimed to remove the small homogeneous vortices and

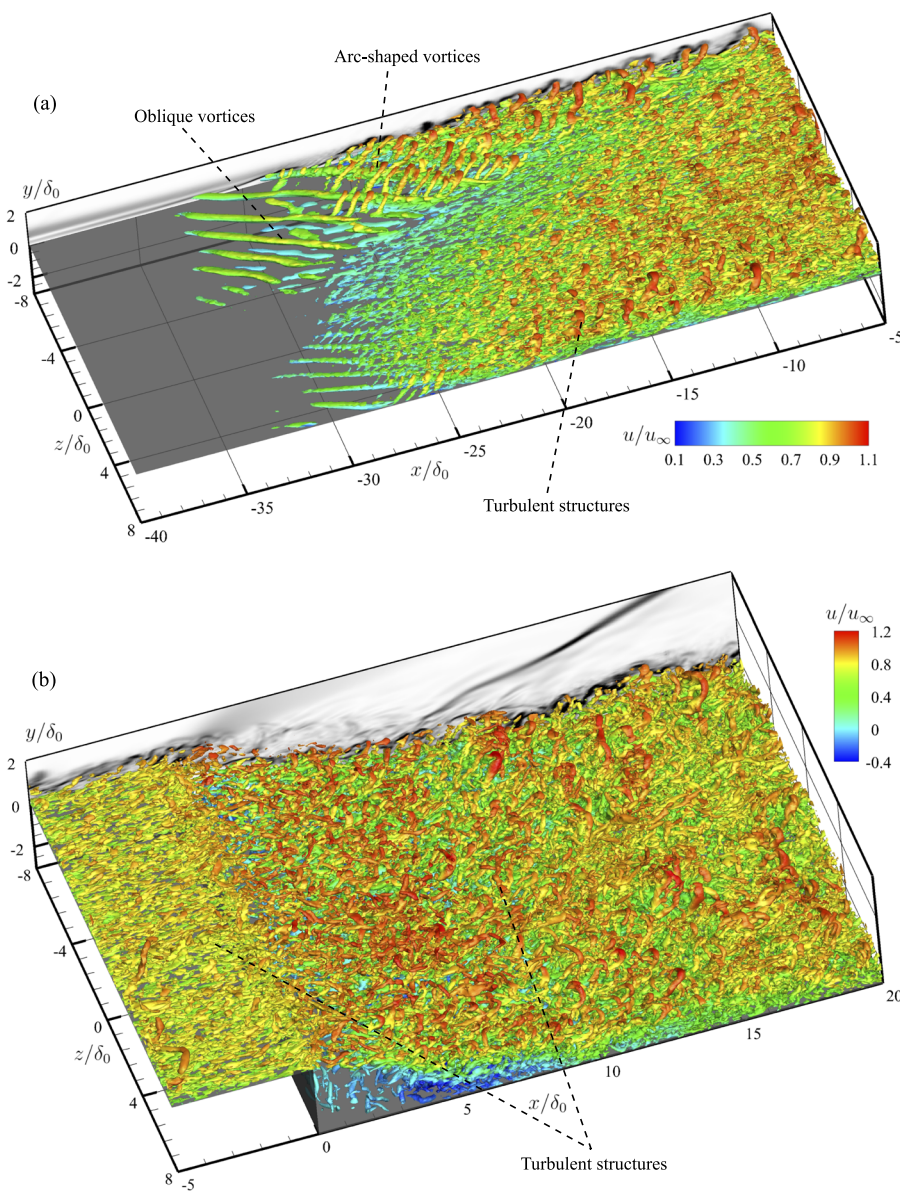


FIG. 7. Instantaneous vortical structures at $u_\infty/\delta_0 = 912$ for case HA, visualized by isosurfaces of λ_2 . A numerical schlieren based on the $z = 0$ slice is also included with $|\nabla \rho|/\rho_\infty = 0-1.4$. (a) Upstream the step at $\lambda_2 = -0.02$ and (b) downstream at $\lambda_2 = -0.08$.

better visualize the interesting vortical structures. The shear layer reattaches earlier because of the more energetic shear layer, while the generated reattachment shock has a smaller shock angle and stronger intensity (see the included numerical schlieren in Fig. 7). The latter observations are in qualitative agreement with the predictions from a theoretical inviscid model of the flow reattachment configuration.

By comparison, the transition path of case LA is very similar to what was observed in the undisturbed laminar case.²³ Basically, the transition consists of four major phases according to the dominant instability. The growth of the T–S modes is the main source of the disturbances upstream the step (phase 1: $x/\delta_0 < 0$). In the second phase (phase 2: $0 \leq x/\delta_0 \leq 4$), the development of large K–H vortices is the most significant feature of the flow field. However, in the current LA simulation case, we can also observe the effect of the oblique waves in this region, such as the harmonic undulation of the K–H vortices compared to the more straight K–H vortices in case ZA. The secondary instability dominates the growth of the turbulence in the third phase (phase 3: $4 \leq x/\delta_0 \leq 7.5$). Near the reattachment location, the breakdown of vortices promotes the transition to fully developed turbulence (phase 4: $x/\delta_0 \geq 7.5$). For case HA, on the other hand, the gradual growth of the oblique T–S waves appears to saturate soon, and other instabilities already take effect well upstream of the step. As a result, the flow field is highly turbulent in the shear layer, which may be the cause that the initiation of large K–H vortices is suppressed. Therefore, with our current interest lying on the interaction between K–H and T–S instabilities, for the subsequent analysis, we identify case LA as the most interesting one to scrutinize the effects of possible primary and secondary instability interactions in the transition for the supersonic BFS configuration.

B. Evolution of instabilities in case LA

1. Tollmien–Schlichting instability

The wavenumber and frequency of the least stable waves depend on the local Reynolds number Re_l based on the Blasius

length.¹⁰ We traced the eigenvalues of the unstable modes, including the least unstable one, along the streamwise direction. The stability diagram is displayed in Fig. 8, where three levels of α_i^l are computed at a constant spanwise wavenumber $\beta^l = 0.06202$ and angular frequency $\omega^l = 0.01605$ against Re_l . Since the Reynolds number of our case is very close to the critical one, the variation of ω is relatively small for each level of α_i^l when $Re_l < 2225$ at $\beta^l = 0.06202$ [Fig. 8(a)]. For increasing Re_l (moving downstream), the upper and lower branches of the stability diagram move toward each other until they finally meet. The unstable region of the oblique waves is decreasing with increasing Re_l and $|\alpha_i^l|$. Figure 8(b) shows the same levels of α_i^l with different Re_l and β^l at a specific angular frequency $\omega^l = 0.01605$. A similar trend of β^l with Re_l is observed as that of ω^l in Fig. 8(a). The development of the most unstable mode (the one with maximum $|\alpha_i^l|$) at the given β^l and ω^l is also included in Fig. 8 (the dashed–dotted lines). We can see that the frequency and spanwise wavenumber of the least unstable modes are relatively constant along the streamwise distance. In conclusion, the wavenumber and frequency of the oblique wave imposed at the inlet remain in the unstable region and are very close to the values of the local most unstable oblique T–S wave upstream the step. Therefore, in the following discussion, we only look into the spatial development of the unstable mode with the imposed wavenumber and frequency using both LST and LES.

The evolution of the oblique waves computed by LES can be measured by the maximum root mean square of the streamwise velocity fluctuations. The semi-log plot in Fig. 9 already indicates that the current LES can well predict the exponential growth rate of the oblique T–S waves. The averaged streamwise growth rate is given by the slope of the curve whose value approximates to 0.0155 and is very close to the LST result $\alpha_\delta = 0.0161$ for the inflow perturbation. We also provide the shape factor of the boundary layer in Fig. 9 (dashed line). The shape factor is almost a constant upstream the step, and its mean value is equal to 4.36. Chang *et al.*⁵³ proposed that the shape factor is a function of pressure gradient and free stream Mach number in a compressible laminar flow with adiabatic wall

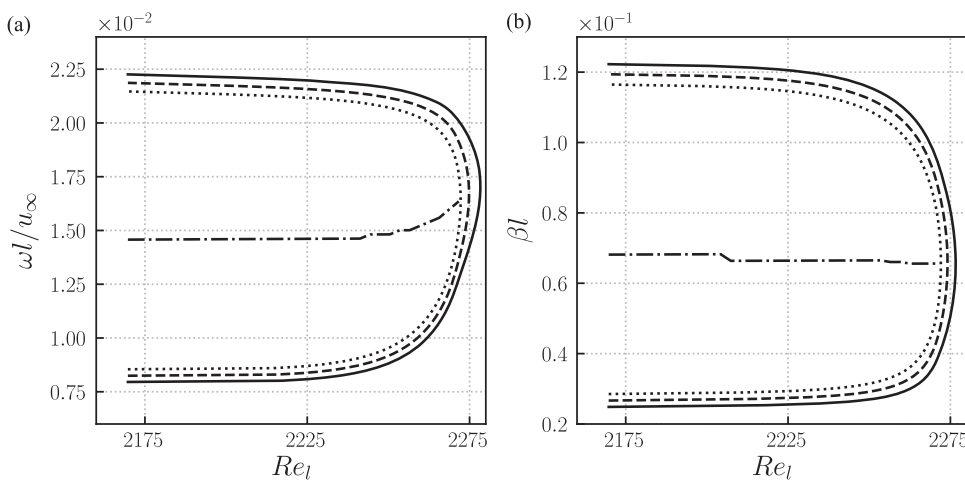


FIG. 8. Contours of α_i^l computed from LST at the imposed (a) spanwise wavenumber $\beta^l = 0.06202$ and (b) angular frequency $\omega^l = 0.01605$ (—, $\alpha_i^l = -0.0014$; - - - - , $\alpha_i^l = -0.0015$; ····, $\alpha_i^l = -0.0016$; and - · - ·, $|\alpha_i^l|_{\max}$).

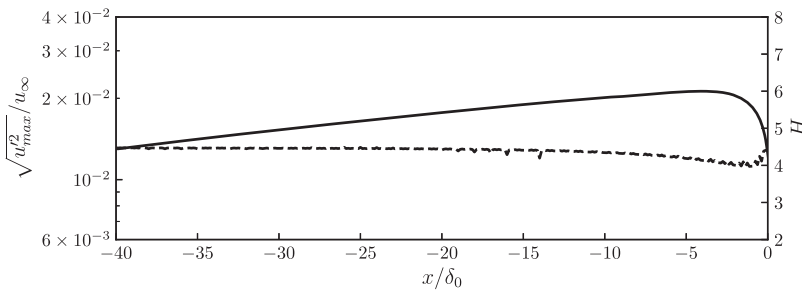


FIG. 9. Maximum rms of streamwise velocity fluctuations (solid line) and shape factor of the boundary layer (dashed line) along the streamwise direction.

and provided the following empirical fit:

$$H(Ma_\infty, \lambda'_\theta) = \frac{3.182\lambda'_\theta + 0.57757}{\lambda'^2_\theta + 1.49\lambda'_\theta + 0.223} \cdot \left(1 + \frac{\gamma - 1}{2} Ma_\infty^2\right), \quad (12)$$

where λ_θ is a corrected pressure gradient factor in compressible flow, which equals to zero in our case without pressure gradient. We obtain $H = 4.09$ using this empirical formula, which is close to the current mean shape factor.

Next, we calculate the streamwise wavenumber and growth rate using LES results. The temporal Fourier transform of the LES data is computed at every streamwise location,

$$Q'(x, f) = \sum_{k=1}^N q'(x, t_k) e^{ift_k}, \quad (13)$$

where t_k denotes the discrete time samples. In the present case, the extracted signals are from the wall pressure and include 1200 samples within five periods of the imposed oblique waves. Next, the corresponding phase angle $\theta(x)$ and amplitude $A(x)$ of the perturbation q' are obtained via

$$\begin{cases} \theta = \arctan \frac{\Im(Q')}{\Re(Q')} \\ A = \|Q'\|. \end{cases} \quad (14)$$

After $\theta(x)$ and $A(x)$ are collected at every streamwise location, the streamwise wave number and growth rate finally are determined

by^{54,55}

$$\begin{cases} \alpha_r(x) = \frac{\partial \theta(x)}{\partial x} \\ \alpha_i(x) = -\frac{1}{A(x)} \frac{\partial A(x)}{\partial x}. \end{cases} \quad (15)$$

The obtained results are compared with the results from LST in Fig. 10. The LES results give a slightly oscillating wave number and growth rates upstream the step ($x/\delta_0 < -10.0$). This modulation usually happens when the forcing amplitude is relatively large and is caused by weak acoustic disturbances traveling within the boundary layer.^{11,54} Near the step, the large variation of α_r and α_i is caused by the non-parallel effects and acceleration in front of the step. We are very satisfied with the agreement of LST and LES.

For further comparisons, the wall-normal amplitude distributions for streamwise velocity and pressure fluctuations are plotted for both LST and LES in Fig. 11, at $x/\delta_0 = -25.0$, $\beta_l = 0.062$, and $\omega_l = 0.016$. The values of all variables are normalized by their respective maximum value of the profiles. Results from these two techniques are found to be in excellent agreement. It manifests that our current LES can reproduce the exponential growth of the oblique T-S waves predicted by LST in the present study. Therefore, we are confident that the well-resolved LES is a suitable method for computing the spatial evolution of these T-S waves downstream.

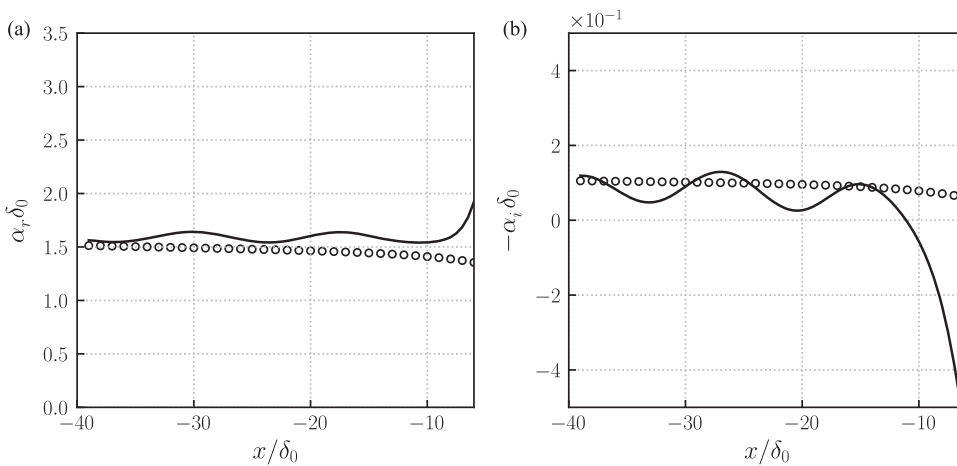


FIG. 10. Streamwise development of (a) wavenumber α_r and (b) growth rate α_i resulting from LST (○) and LES (—).

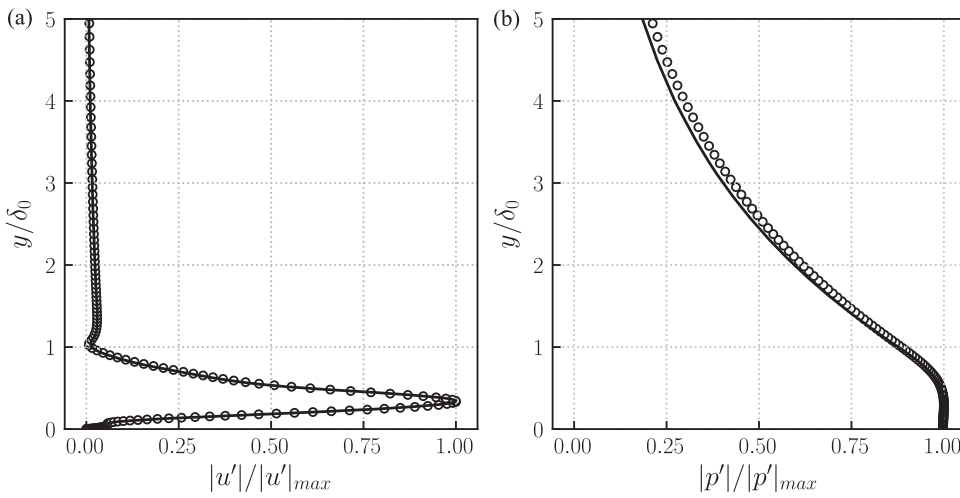


FIG. 11. Comparison of wall-normal profiles of perturbation amplitudes between LST (\circ) and LES (—) for (a) stream-wise velocity and (b) pressure at $x/\delta_0 = -25.0$, $\beta_1 = 0.062$, and $\omega_1 = 0.016$ for case LA.

2. Primary Kelvin-Helmholtz instability

The incoming laminar boundary layer separates at the step edge upon which a strong initially two-dimensional shear layer is generated (see Fig. 6). The spanwise vorticity propagates and redistributes along the free shear layer via the K-H instability. Immediately downstream the step, two-dimensional vortices are produced due to the K-H instability, which is absolutely unstable to small disturbances, such as incoming T-S waves and the additional effect of the small numerical round-off errors. Then, these two-dimensional waves undergo deformation and distortion caused by the growing

disturbances. In the meantime, the region of strong spanwise vorticity gradually expands and simultaneously vorticity peaks develop at certain locations where the quasi-two-dimensional K-H vortices are formed. These spanwise vortical structures behind the step are also visualized by the pressure contours of spanwise-normal slices in Fig. 12. The vortex lines (black) point to the negative spanwise direction, corresponding to clockwise rotation looking from the left side. In case ZA, the vortex lines are straight in the spanwise direction, whereas these lines are sinusoidal due to the incoming oblique T-S waves in case LA, corresponding to the harmonic undulation of the K-H vortices in Fig. 6(b).

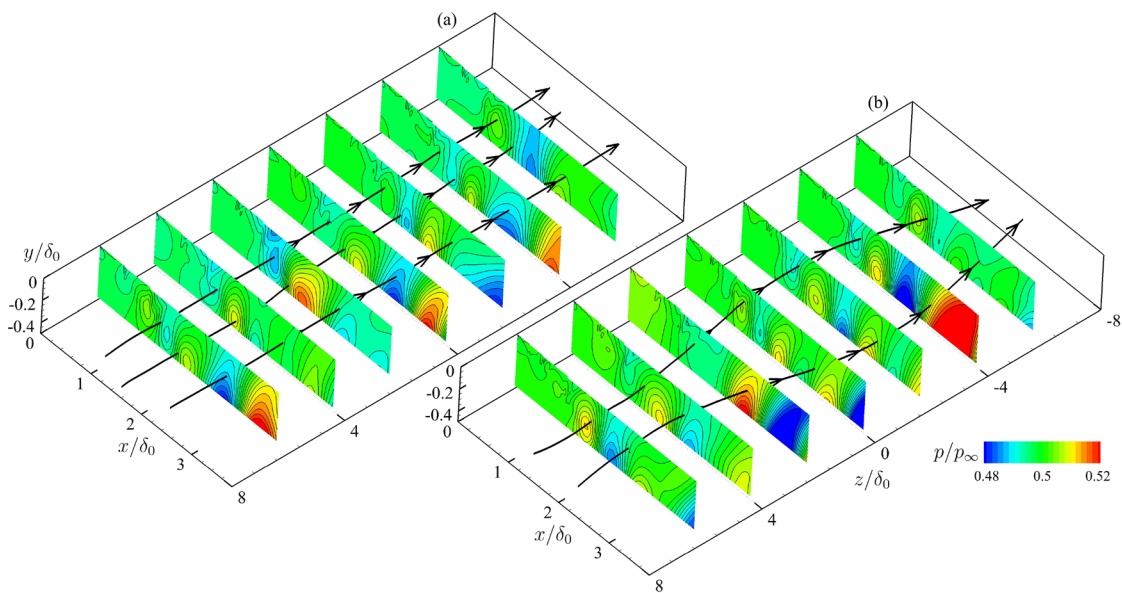


FIG. 12. K-H vortices illustrated by contours of pressure at $t u_\infty/\delta_0 = 912$. Black arrow lines represent the vortex lines. (a) Case ZA and (b) case LA.

In Secs. III B 2-III B 4, we provide a further analysis of the involved instabilities from the perspective of vorticity dynamics. By analyzing the generation, development, and structural characteristics of the vorticity, such as stretching, tilting, and lift up, in the transition process, we obtain an understanding of how the primary instability evolves and the secondary instability is excited. The enstrophy is defined as the integral of the square of the vorticity,

$$\mathcal{E} = \int_A \frac{1}{2} \omega_i \omega_i dA, \tag{16}$$

where A is the area of the cross section perpendicular to the streamwise direction. Hiejima⁵⁶ has used this variable to quantify the streamwise location of the vortex breakdown in the transition process induced by supersonic streamwise vortices. For compressible flow, the transport equation for the local enstrophy is formulated as⁵⁷

$$\begin{aligned} \frac{d}{dt} \left(\frac{1}{2} \omega_i^2 \right) = & \underbrace{\omega_i \omega_j \frac{\partial u_i}{\partial x_j}}_{T+S} - \underbrace{\omega_i^2 \frac{\partial u_j}{\partial x_j}}_D + \underbrace{\varepsilon_{ijk} \frac{\omega_i}{\rho^2} \frac{\partial \rho}{\partial x_j} \frac{\partial p}{\partial x_k}}_B \\ & + \underbrace{\omega_i \varepsilon_{ijk} \frac{\partial}{\partial x_j} \left(\frac{1}{\rho} \frac{\partial \tau_{kl}}{\partial x_l} \right)}_V. \end{aligned} \tag{17}$$

The first term can be decomposed into three parts, for instance for the x direction,

$$\begin{aligned} T &= T_{xy} + T_{xz} = \frac{\partial u}{\partial y} \omega_y \omega_x + \frac{\partial u}{\partial z} \omega_z \omega_x, \\ S_{xx} &= \frac{\partial u}{\partial x} \omega_x \omega_x, \end{aligned} \tag{18}$$

where the first two terms T_{xy} and T_{xz} represent the vortex tilting caused by the wall-normal and spanwise vorticity, while S specifies the vortex stretching. The second term D represents the dilation effects in compressible flows. The function of this term is to redistribute the existing vorticity, instead of creating or destroying. In response to this term, the local enstrophy decreases if the flow field is undergoing expansion, and it increases in compression regions. Terms B and V signify the baroclinic torque and viscous dissipation, respectively. If the density gradient and pressure gradient are nearly parallel in the flow field, the baroclinic torque is negligible. In a high speed flow, especially when a large-scale vortex structure occurs, viscous dissipation can be neglected due to the

high Re . For this reason, V will not be considered in the following analysis. The evolution of the instabilities and underlying vortical mechanism can be scrutinized by assessing the contribution of each term in the enstrophy transport equation. Suryanarayanan, Goldstein, and Brown⁵⁸ enhanced the mechanistic understanding of the transition process induced by discrete roughness elements based on this vorticity-based analysis.

The streamwise distribution of the integral enstrophy is computed using Eq. (16) for the three individual coordinate directions, as well as for the total enstrophy, with the results, as shown in Fig. 13. The integration area is selected as $-8.0 \leq z/\delta_0 \leq 8.0$ and $-3.0 \leq y/\delta_0 \leq 0.0$, where most of the vortical activity occurs. At the step ($x/\delta_0 = 0$), the large spanwise enstrophy component is caused by the strong inviscid instability of the shear layer. The total enstrophy subsequently decays and reaches a minimum at $x/\delta_0 \approx 2.5$ due to the spatial redistribution of the spanwise vorticity (as will be shown in Fig. 16). The total enstrophy increases gradually with the streamwise distance in the second phase between $2.5 < x/\delta_0 < 7.5$ mainly due to the evolution of spanwise and streamwise vorticity. Then, the enstrophy remains at a high and relatively constant level in the vortex breakdown and reattachment region ($7.5 < x/\delta_0 < 14.0$). This observation provides supporting evidence that the vortex breakdown usually occurs in the vicinity of the location where a local maximum of enstrophy is present.⁵⁶ The spanwise enstrophy \mathcal{E}_z is the most significant one in the region of $0.0 < x/\delta_0 < 5.0$, and then again in the downstream region $x/\delta_0 > 15.0$.

Using the decomposition according to the separate terms in Eqs. (17) and (18), the balance of the most important enstrophy \mathcal{E}_z and its evolution along the streamwise direction is shown in Fig. 14. The integration area in the y - z plane is the same as for Fig. 13. The dilatation term is the most significant contribution near the step, which is expected because the vorticity field is subject to a strong expansion.

For $2.5 < x/\delta_0 < 4.0$, the development of the vorticity field is dominated by S_{zz} , i.e., the vortex stretching of the induced K-H vortices, caused by the gradient of the spanwise velocity $\partial w/\partial z$. Based on the above vortex visualization and vorticity dynamics analysis, the most significant disturbances are the K-H vortices in this stage, and the development of the eddies is mainly due to the dilation and stretching of the spanwise vorticity itself. It can be inferred that the primary K-H instability plays the most important role in this process, instead of T-S and secondary instabilities.

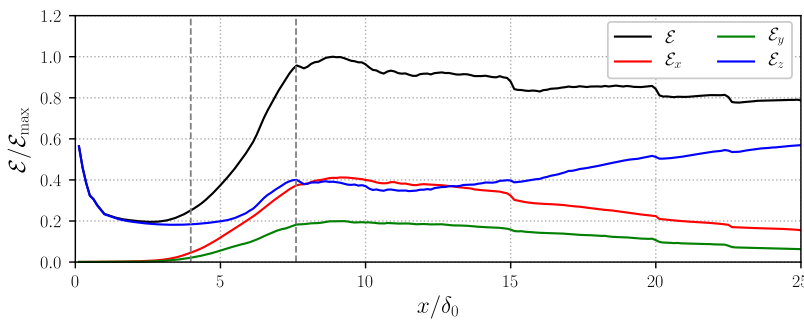


FIG. 13. Streamwise development of the integrated enstrophy in the y - z plane for case LA. The gray dashed lines distinguish the different phases in the transition process.

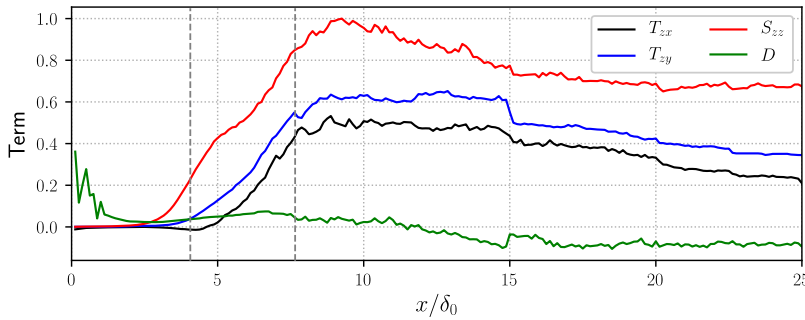


FIG. 14. Streamwise variation of the integrated production terms for S_{zz} behind the step for case LA. The gray dashed lines distinguish the different phases in the transition process.

Although the T-S waves are not clearly visible in Fig. 12, they still coexist with the K-H modes in the second phase. They do not show up prominently in the visualization because T-S waves only have a weak velocity gradient, which is overwhelmed by the strong contribution of the K-H vortices. To better assess the development of the T-S waves, three stations have been selected (one just upstream of the step and two in the separated shear layer downstream of it) to analyze the spatial evolution of the wave pattern across the step. Figure 15 provides the signals of the streamwise velocity at these stations alongside with their frequency weighted power spectral density. Compared with case ZA, case LA shows large amplitude fluctuations and a single dominant frequency peak at $f\delta_0/u_\infty \approx 0.016$ for station A, corresponding to the amplitude and

frequency of the imposed oblique waves. Shortly downstream (station B), the sinusoidal footprint of the oblique waves can still be recognized, but it is mixed with higher frequency fluctuations. At the same time, it is observed that the oblique waves are strongly amplified, and their energy is about 20 times larger than at the upstream station A. In this small region, the original information of the T-S waves can be extracted with the amplified amplitude by a low-pass filter since the interacting signals are not strongly coupled yet. Further downstream (station C), the velocity fluctuations exhibit a wide-band frequency spectrum. The most significant peak is at $f\delta_0/u_\infty \approx 0.2$, which corresponds to the natural frequency of the K-H vortices for the current configuration.²³ The fluctuation energy of case LA is still larger than for case ZA, for example, around

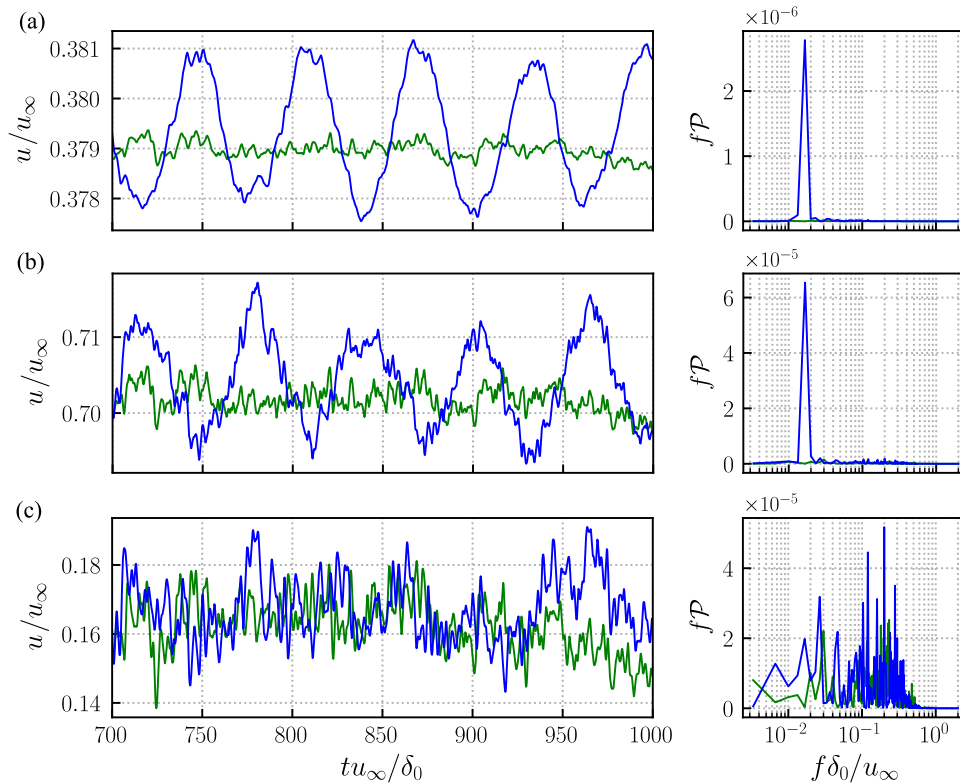


FIG. 15. Temporal evolution of the streamwise velocity perturbations (left) and the corresponding frequency weighted power spectral density (right) at (a) station A ($x/\delta_0 = -0.1875$, $y/\delta_0 = 0.03125$), (b) station B ($x/\delta_0 = 0.203125$, $y/\delta_0 = 0.0390625$), and (c) station C ($x/\delta_0 = 0.59375$, $y/\delta_0 = -0.171875$) based on the slice $z = 0$ for case ZA (green lines) and LA (blue lines).

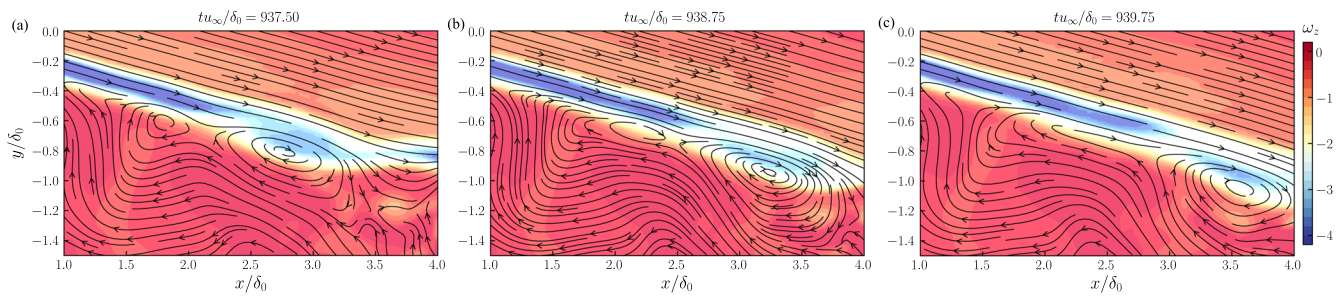


FIG. 16. Contour of spanwise vorticity with the streamlines in the x - y plane at three instants, showing the K-H vortex pairing.

two times larger at $f\delta_0/u_\infty = 0.2$. Additionally, the incoming T-S waves and intrinsic K-H waves are fully coupled already without a significant low-frequency feature of the T-S waves. Therefore, we believe that the K-H instability acts as an amplifier of the incoming weak oblique waves and spanwise K-H waves themselves in the interaction between primary T-S and K-H modes.^{59,60}

On the other hand, the spanwise wavenumber modulation also contributes to the interaction. As shown in Fig. 6(b), the large quasi-two-dimensional K-H vortices are undulated in the shape of the incoming T-S waves along the spanwise direction between $2.0 < x/\delta_0 < 3.0$. Compared to the straight vortex lines in case ZA [Fig. 12(a)], the vortex lines of case LA present harmonic (sinusoidal) wave forms with the spanwise wavelength of the incoming T-S waves [Fig. 12(b)]. The vortex pairing may occur with the mutual

interaction of the neighboring wavy vortices, as well as the convected shear layer. The vortex merging process is visualized by the streamlines in Fig. 16. At the initialization phase of the vortex pairing, the upstream K-H vortices are slightly weaker and smaller [Fig. 16(a)]. As both of the vortices are advected downstream, the weaker vortices cannot resist the stronger strain field generated by the other one and are stretched by the velocity gradient [Fig. 16(b)]. Finally, the upstream vortices are striped off from the downstream outer recirculation region and merged into the stronger one during the convection process [Fig. 16(c)].^{61,62}

In the weak coupling region, both of the T-S and K-H modes are the primary mode. The growth rate of the fluctuations caused by them is examined in Fig. 17(a). In a very short distance ($0 < x/\delta_0 < 0.8$), the growth rate of existing waves within the shear layer falls

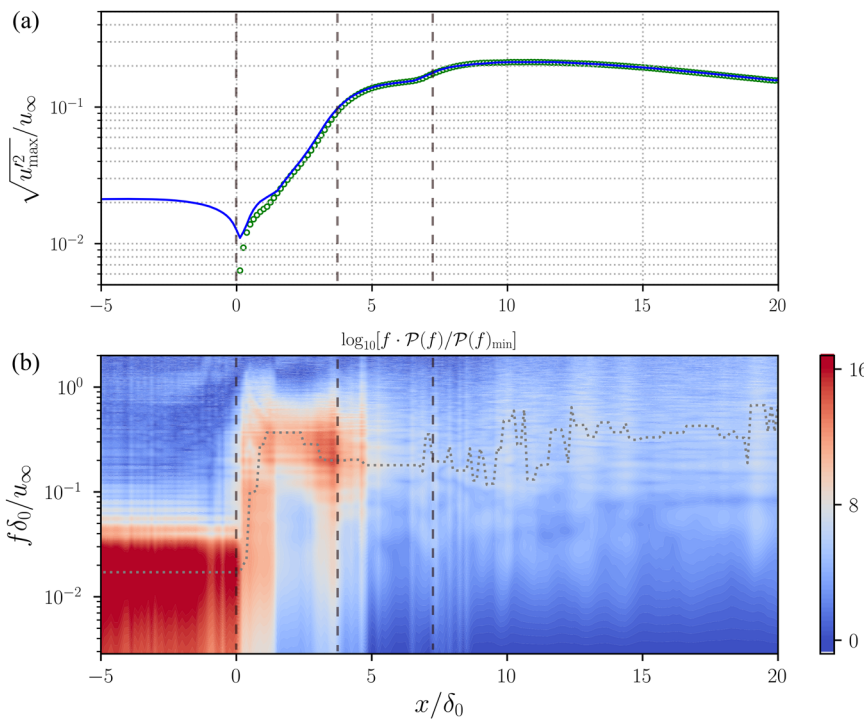


FIG. 17. (a) Maximum rms of streamwise velocity fluctuations along the streamwise direction (case ZA, green circle; case LA, blue solid line) and (b) frequency weighted power spectral density map of maximum pressure signals along the streamwise direction based on the $z = 0$ slice between $-5.0 \leq x/\delta_0 \leq 20.0$ for case LA. At every streamwise position, the weighted spectra are normalized by the minimum of $\mathcal{P}(f)$. The gray dotted line signifies the frequency at which $f\mathcal{P}(f)$ is maximum. The gray dashed lines distinguish the different phases in the transition process.

into a quasi-linear regime, but with a much larger value compared to the growth rate of the upstream T–S waves. Wu, Ma, and Zhou⁵⁷ also reported the linear growing behavior of the K–H waves in the early roll-up process of the large K–H vortex. In contrast, the small disturbances (around $10^{-6}u_\infty$) upstream the step in case ZA are drastically amplified in the redistribution region of the spanwise vorticity. Once the spanwise K–H vortices emerge, both cases ZA and LA display a similar level of fluctuations in the shear layer. The dominant frequency of the unsteady waves shifts from the low value ($f\delta_0/u_\infty \approx 0.016$) to a much higher one ($f\delta_0/u_\infty \approx 0.2 \sim 0.4$), which suggests the leading instability switching from the T–S instability to the K–H instability, as shown in Fig. 17(b). When the maximum amplitude of the fluctuations exceeds $2\%u_\infty$, the K–H mode plays a more important role and undergoes a rapid growth ($0.8 < x/\delta_0 < 4.0$). We infer that the dilatation of the spanwise vorticity has a greater effect on the high-frequency waves caused by the shear layer instability than on the low-frequency oblique waves. Subharmonic K–H waves are produced between $2.5 < x/\delta_0 < 4.0$ due to the vortex pairing of the fundamental K–H vortices, which reduces the leading frequency to $f\delta_0/u_\infty \approx 0.2$.

3. Secondary instability

The velocity is not uniform along the spanwise direction, and the K–H vortices are not strictly two dimensional in the shear layer, which induces two types of secondary instabilities in the transition. As shown in Fig. 13, there is significant creation of wall-normal and streamwise vorticity after the first phase ($x/\delta_0 \geq 4.0$). First of all, the wall-normal velocity is non-uniform in the spanwise direction due to the existing disturbances within the shear layer. The originally spanwise-aligned vortices may then be lifted up at some locations where there is high wall-normal velocity. These high-velocity regions are obvious in the instantaneous vortical structures visualization of Fig. 18(a). This secondary lift-up effect produces wall-normal vorticity. As shown in Fig. 18(d), the coherent vortices are gradually lifted up in the streamwise direction. If we consider the enstrophy balance for the wall-normal direction (Fig. 19), it is obvious that the upward tilting of spanwise vorticity is the dominant mechanism in producing the wall-normal vorticity.

Moreover, the bent-up parts of the vortices are convected faster than the other parts due to the larger streamwise velocity in the

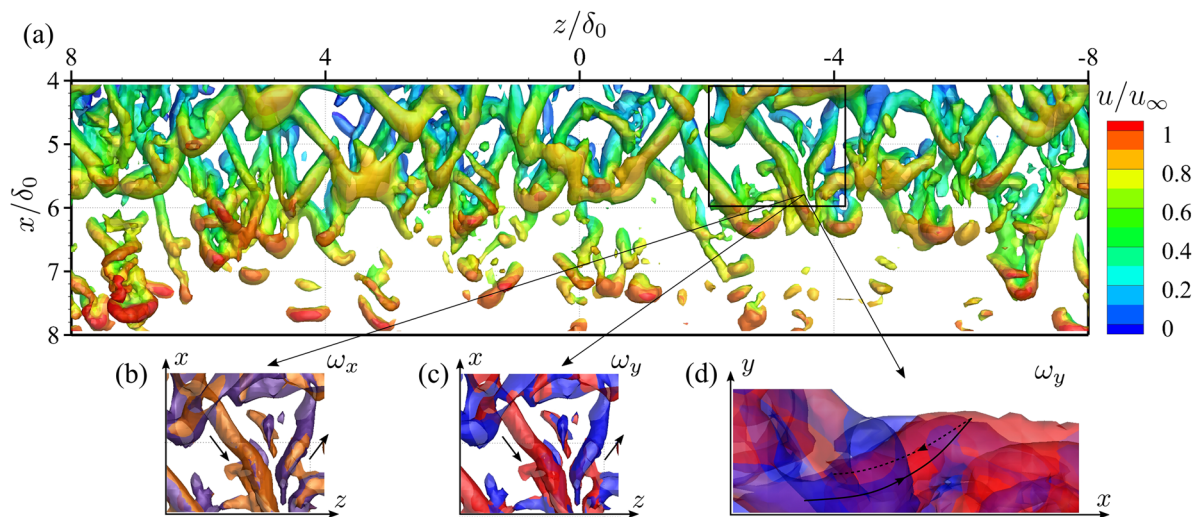


FIG. 18. Isosurfaces of vortical criterion $Q = 0.08$ at $tu_\infty/\delta_0 = 912$, contoured by (a) streamwise velocity, (b) streamwise vorticity (purple: $\omega_x < 0$; orange: $\omega_x > 0$), (c) wall-normal vorticity, and (d) wall-normal vorticity in the x – y plane (blue: $\omega_y < 0$; red: $\omega_y > 0$).

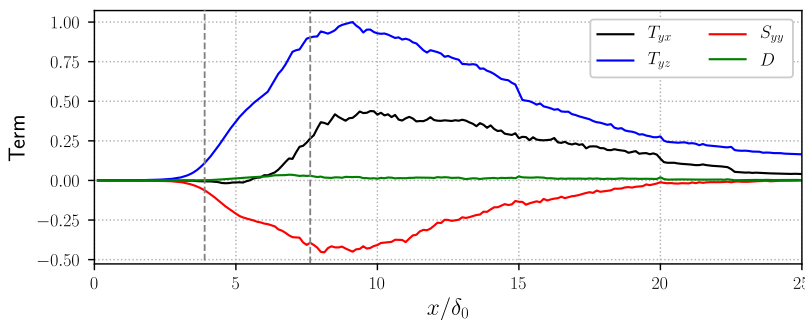


FIG. 19. Streamwise variation of the integrated production terms for \mathcal{E}_y behind the step for case LA. The gray dashed lines distinguish the different phases in the transition process.

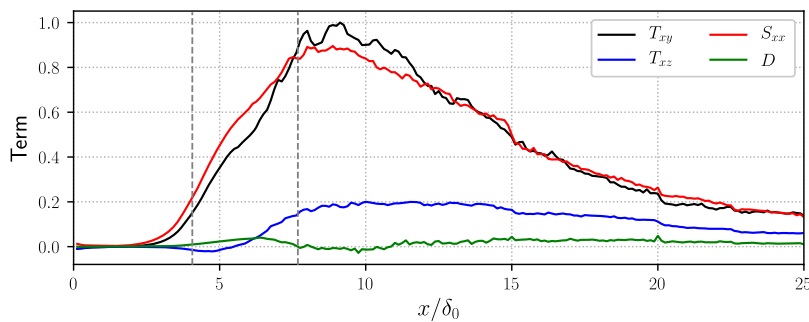


FIG. 20. Streamwise variation of the integrated production terms for \mathcal{E}_x behind the step for case LA. The gray dashed lines distinguish the different phases in the transition process.

upper region of the shear layer. This secondary behavior leads to the nonuniformity of the streamwise velocity in the spanwise direction, which generates streamwise vorticity. By the analysis of the enstrophy balance for the x -direction (Fig. 20), we can see that the tilting of wall-normal vortices is a significant contributor to increase the streamwise vorticity. In turn, the streamwise velocity gradient along the induced vortex line $\partial u/\partial x$ leads to the stretching of the streamwise vortices, which is also the main mechanism for the enstrophy evolution in this stage.

The combination of these two secondary instabilities results in the initiation of the large Λ -shaped vortices (see Fig. 18) in which high-speed parts of the spanwise vortices are elevated by the secondary lift-up effects and subsequently the streamwise vorticity is produced due to the secondary streamwise tilting dynamics. The low-momentum parts form into the legs of the Λ -shaped vortices, and the high-momentum parts develop into the head of Λ -shaped vortices in this region. Since the strong spanwise vorticity has a negative sign, the left leg of the Λ -shaped vortex has positive streamwise [Fig. 18(b)] and wall-normal [Fig. 18(c)] vorticity, while the right leg has negative vorticity. As long as the streamwise vortices are produced, they will keep stretching because of the higher speed in the bending parts until they break down. In general, the streamwise enstrophy is more significant than the wall-normal enstrophy in this stage (see Fig. 13).

As shown in Fig. 17, the secondary instability undergoes a rapid growth to $20\%u_\infty$ in this stage and the frequency characteristic shifts from a dominant value $f\delta_0/u_\infty \approx 0.2$, the same value of subharmonic

K–H waves, to a low-frequency broadband spectrum, which is also reported by Sansica, Sandham, and Hu⁶³ in their shock-induced laminar separation bubble case. The unsteadiness of the primary T–S modes is much less energetic than that of the subharmonic waves. We believe that the primary T–S waves appear to be contaminated or retarded. Our observations support the opinion that the primary T–S waves diminish in the region where the excited secondary disturbances have a large amplitude.⁵⁴ The dominant mechanism is the slow resonance between subharmonic K–H vortices and the secondary instability in this region in which disturbances slowly grow due to the induced secondary instability and their frequency features still remain the same as those of subharmonic K–H vortices.

4. Breakdown and reattachment

In the following stage ($x/\delta_0 \geq 7.5$), the streamwise vortices keep being elongated in the streamwise direction and lifted up due to stretching dynamics (see Figs. 19 and 20). This rolling up and prolongation lead to the formation of the small hairpin vortices, which is the signature of a fully developed turbulent flow, as illustrated in Fig. 21. The enstrophy reaches its global maximum before the shear flow impinges on the wall, which occurs around $x/\delta_0 = 10.9$. Then, the strong vorticity tilting and stretching terms start to decrease until they vanish gradually far downstream. Across the reattachment, the hairpin vortices keep their typical structure, apparently without significant effects from the compression waves in their proximity. The streamwise and spanwise spacing of the hairpin vortices is $\lambda_x \approx \lambda_z$

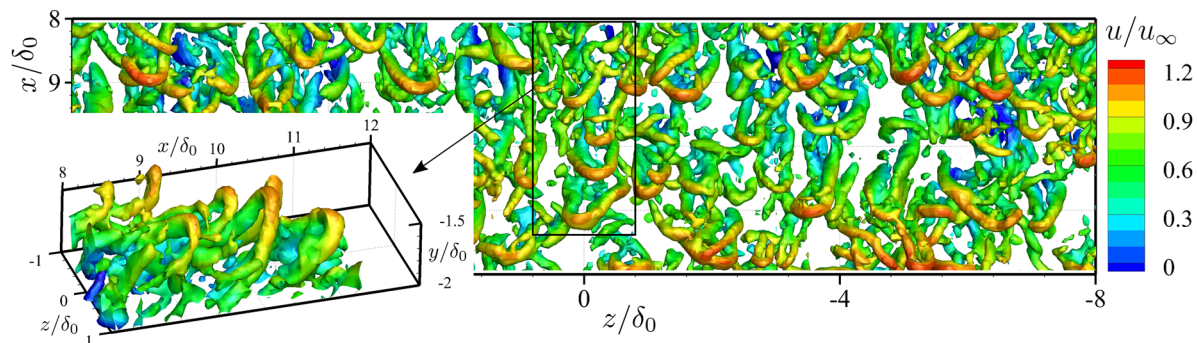


FIG. 21. Isosurfaces of vortical criterion $\lambda_2 = -0.1$ at $t u_\infty/\delta_0 = 908$ contoured by the streamwise velocity.

$\approx 90v/u_\tau$ based on the local wall shear stress, which is the typical spacing of the coherent structures, as reported in previous experimental studies.⁶⁴ The fluctuations of velocity reach their highest level at the mean reattachment point, as shown in Fig. 17(a). The pressure power spectral density [Fig. 17(b)] shows a broadband distribution typical for developed turbulence. In addition, more energy is observed around the reattachment in the low-frequency parts ($f\delta_0/u_\infty \approx 0.2$).

In summary, the imposed low-amplitude oblique waves undergo slow growth in agreement with the expected linear dynamics upstream the step and damp close to the step due to the expansion fan. In a short distance behind the step, both oblique T-S waves and generated K-H waves act as the primary mode. The interaction of T-S and K-H waves leads to the rapid growth of the disturbances within $0 \leq x/\delta_0 \leq 1$. Pairing of the adjacent undulating K-H vortices generates subharmonic K-H waves. Then, the large-amplitude secondary instability, including the lift-up effects and streamwise tilting, begins to take the lead. In the meantime, the weak T-S waves vanish in the competition with the strong subharmonic waves and can no longer be discerned. As the flow reattaches downstream, the transition to fully developed three-dimensional turbulence with a broadband frequency spectrum (cf. Fig. 17) is almost completed.

IV. CONCLUSION

The transition path and unsteady behavior of the supersonic flow over a backward-facing step geometry show large differences between the two cases with low- and high-amplitude upstream disturbances. For case HA with high-amplitude initial perturbation, we obtain the excitation of oblique and secondary vortices, as well as non-linear breakdown already upstream of the step. This leads to a turbulent boundary layer upstream of the separation bubble. In contrast, the imposed low-amplitude oblique T-S wave (case LA) remains within the linear growth regime, which is the initial stage of the natural transition. Therefore, the laminar-to-turbulent transition scenario does not differ much from the fully laminar case ZA, i.e., initiation of the K-H instability, followed by the secondary instability, leading to Λ -shaped vortices, hairpin vortices, and finally to a fully turbulent state. In a short distance behind the step, the interaction between T-S and K-H modes is a weak coupling process in which the amplitude of T-S waves is amplified significantly by the strong shear layer, but their frequency remains unchanged. In addition, the spanwise K-H vortices show a harmonic undulation with the wavelength of the T-S wave. Due to the effects of the energetic three-dimensional fluctuations downstream the separation bubble, the interaction enters a non-linear stage and the unsteady behavior features a broad range of space and time scales. Behind the reattachment point, the boundary layer is highly turbulent.

ACKNOWLEDGMENTS

This work was carried out on the Dutch National e-Infrastructure with the support of SURF Cooperative. This work is part of the research programme “Dynamics of a Backward/Forward-Facing Step in a Supersonic Flow” under Project No. 2019.045, which was partly financed by the Dutch Research Council (NWO).

DATA AVAILABILITY

Raw data were generated at a large scale facility, including Dutch National Supercomputer, Cartesius, and the local machine. Derived data supporting the findings of this study are available from the corresponding author upon reasonable request.

REFERENCES

- Y. X. Wang and M. Gaster, “Effect of surface steps on boundary layer transition,” *Exp. Fluids* **39**, 679–686 (2005).
- N. Mendoza and R. Bowersox, “On the unsteady shock wave interaction with a backward-facing step: Inviscid analysis,” in *42nd AIAA Fluid Dynamics Conference and Exhibit* (American Institute of Aeronautics and Astronautics, Reston, Virginia, 2012).
- A. Y. Golubev and D. G. Zhestkov, “Pressure fluctuation fields in front of inclined forward-facing step and behind inclined backward-facing step,” *Russ. Aeronaut.* **57**, 388–394 (2014).
- W. Huang, M. Pourkashanian, L. Ma, D. B. Ingham, S. B. Luo, and Z. G. Wang, “Investigation on the flameholding mechanisms in supersonic flows: Backward-facing step and cavity flameholder,” *J. Visualization* **14**, 63–74 (2011).
- M. Barri, G. K. El Khoury, H. I. Andersson, and B. Pettersen, “DNS of backward-facing step flow with fully turbulent inflow,” *Int. J. Numer. Methods Fluids* **64**, 777–792 (2009).
- H. M. Blackburn, D. Barkley, and S. J. Sherwin, “Convective instability and transient growth in flow over a backward-facing step,” *J. Fluid Mech.* **603**, 271–304 (2008).
- D. Lanzerstorfer and H. C. Kuhlmann, “Global stability of the two-dimensional flow over a backward-facing step,” *J. Fluid Mech.* **693**, 1–27 (2012).
- H. L. Reed, W. S. Saric, and D. Arnal, “Linear Stability theory applied to boundary layers,” *Annu. Rev. Fluid Mech.* **28**, 389–428 (1996).
- M. R. Malik, “Numerical methods for hypersonic boundary layer stability,” *J. Comput. Phys.* **86**, 376–413 (1990).
- F. M. White and I. Corfield, *Viscous Fluid Flow* (McGraw-Hill, New York, 2006), pp. 1–638.
- C. S. J. Mayer, D. A. Von Terzi, and H. F. Fasel, “Direct numerical simulation of complete transition to turbulence via oblique breakdown at Mach 3,” *J. Fluid Mech.* **674**, 5–42 (2011).
- C.-L. Chang and M. R. Malik, “Oblique-mode breakdown and secondary instability in supersonic boundary layers,” *J. Fluid Mech.* **273**, 323–360 (1994).
- Y.-m. Zhang and H. Zhou, “PSE as applied to problems of secondary instability in supersonic boundary layers,” *Appl. Math. Mech.* **29**, 1–8 (2008).
- R. J. Volino and T. W. Simon, “Bypass transition in boundary layers including curvature and favorable pressure gradient effects,” *J. Turbomachinery* **117**, 166–174 (1995).
- G. Balamurugan and A. C. Mandal, “Experiments on localized secondary instability in bypass boundary layer transition,” *J. Fluid Mech.* **817**, 217–263 (2017).
- I. E. Abdalla and Z. Yang, “Numerical study of the instability mechanism in transitional separating-reattaching flow,” *Int. J. Heat Fluid Flow* **25**, 593–605 (2004).
- G. T. Duncan, Jr., “The effects of step excrescences on swept-wing boundary-layer transition,” Ph.D. thesis, Texas A&M University, 2014.
- R. K. Soni, N. Arya, and A. De, “Characterization of turbulent supersonic flow over a backward-facing step,” *AIAA J.* **55**, 1511–1529 (2017).
- J. L. Eppink, R. W. Wlezien, R. A. King, and M. Choudhari, “Interaction of a backward-facing step and crossflow instabilities in boundary-layer transition,” *AIAA J.* **56**, 497–509 (2017).
- J. R. Brinkerhoff and M. I. Yaras, “Interaction of viscous and inviscid instability modes in separation-bubble transition,” *Phys. Fluids* **23**, 124102 (2011).
- P. Balakumar, R. A. King, and J. L. Eppink, “Effects of forward and backward facing steps on the crossflow receptivity and stability in supersonic boundary layers,” AIAA Paper No. 2014-2639, 2014.

- ²²Y. Zhu, S. Yi, D. Gang, and L. He, "Visualisation on supersonic flow over backward-facing step with or without roughness," *J. Turbul.* **16**, 633–649 (2015).
- ²³W. Hu, S. Hickel, and B. van Oudheusden, "Dynamics of a supersonic transitional flow over a backward-facing step," *Phys. Rev. Fluids* **4**, 103904 (2019).
- ²⁴C. S. J. Mayer, S. Wernz, and H. F. Fasel, "Numerical investigation of the non-linear transition regime in a Mach 2 boundary layer," *J. Fluid Mech.* **668**, 113–149 (2011).
- ²⁵O. Marxen, G. Iaccarino, and E. S. G. Shaqfeh, "Nonlinear instability of a supersonic boundary layer with two-dimensional roughness," *J. Fluid Mech.* **752**, 497–520 (2014).
- ²⁶I. I. Lipatov and R. Y. Tugazakov, "Nonlinear instability in the region of laminar-turbulent transition in supersonic three-dimensional flow over a flat plate," *Fluid Dyn.* **53**, 285–295 (2018).
- ²⁷P. Paredes, M. M. Choudhari, and F. Li, "Instability wave-streak interactions in a supersonic boundary layer," *J. Fluid Mech.* **831**, 524–553 (2017).
- ²⁸D. V. Khotyanovsky and A. N. Kudryavtsev, "Direct numerical simulation of the transition to turbulence in a supersonic boundary layer on smooth and rough surfaces," *J. Appl. Mech. Tech. Phys.* **58**, 826–836 (2017).
- ²⁹S. Hickel, C. P. Egerer, and J. Larsson, "Subgrid-scale modeling for implicit large eddy simulation of compressible flows and shock-turbulence interaction," *Phys. Fluids* **26**, 106101 (2014).
- ³⁰S. Gottlieb and C.-W. Shu, "Total variation diminishing Runge-Kutta schemes," *Math. Comput.* **67**, 73–85 (1998).
- ³¹M. Grilli, P. J. Schmid, S. Hickel, and N. A. Adams, "Analysis of unsteady behaviour in shockwave turbulent boundary layer interaction," *J. Fluid Mech.* **700**, 16–28 (2012).
- ³²J. Matheis and S. Hickel, "On the transition between regular and irregular shock patterns of shock-wave/boundary-layer interactions," *J. Fluid Mech.* **776**, 200–234 (2015).
- ³³V. Pasquariello, S. Hickel, and N. A. Adams, "Unsteady effects of strong shock-wave/boundary-layer interaction at high Reynolds number," *J. Fluid Mech.* **823**, 617–657 (2017).
- ³⁴S. Hickel, N. A. Adams, and J. A. Domaradzki, "An adaptive local deconvolution method for implicit LES," *J. Comput. Phys.* **213**, 413–436 (2006).
- ³⁵T. Herbert, "Parabolized stability equations," *Annu. Rev. Fluid Mech.* **29**, 245–283 (1997).
- ³⁶J. Wang, P. Ziadé, G. Huang, and P. E. Sullivan, "Bi-global stability analysis in curvilinear coordinates," *Phys. Fluids* **31**, 105105 (2019).
- ³⁷F. Pinna, "Numerical study of stability of flows from low to high Mach number," Ph.D. thesis, von Karman Institute for Fluid Dynamics, 2011.
- ³⁸K. Groot, "Derivation of and Simulations with biGlobal stability equations," M.Sc. thesis, Delft University of Technology, 2013.
- ³⁹J. Serpieri and M. Kotsonis, "Three-dimensional organisation of primary and secondary crossflow instability," *J. Fluid Mech.* **799**, 200–245 (2016).
- ⁴⁰J. Casacuberta, K. J. Groot, H. J. Tol, and S. Hickel, "Effectivity and efficiency of selective frequency damping for the computation of unstable steady-state solutions," *J. Comput. Phys.* **375**, 481–497 (2018).
- ⁴¹L. M. Mack, "Linear stability theory and the problem of supersonic boundary-layer transition," *AIAA J.* **13**, 278–289 (1975).
- ⁴²L. M. Mack, "Boundary-layer linear stability theory," AGARD Report No. 709, North Atlantic Treaty Organization, 1984.
- ⁴³A. Tumin, "Three-dimensional spatial normal modes in compressible boundary layers," *J. Fluid Mech.* **586**, 295–322 (2007).
- ⁴⁴P. Balakumar and M. R. Malik, "Discrete modes and continuous spectra in supersonic boundary layers," *J. Fluid Mech.* **239**, 631–656 (1992).
- ⁴⁵S. Pirozzoli, F. Grasso, and T. B. Gatski, "Direct numerical simulation and analysis of a spatially evolving supersonic turbulent boundary layer at $M = 2.25$," *Phys. Fluids* **16**, 530–545 (2004).
- ⁴⁶A. Karimi, S. Wijeyakulasuriya, and M. Nalim, "Numerical study of supersonic flow over backward-facing step for scramjet application," in *48th AIAA/ASME/SAE/ASEE Joint Propulsion Conference & Exhibit* (AIAA J, Atlanta, Georgia, 2012), pp. 1–14.
- ⁴⁷K. Chakravarthy, K. Arora, and D. Chakraborty, "Use of digitally filtered inflow conditions for LES of flows over backward facing steps," *Eur. J. Mech., B/Fluids* **67**, 404–416 (2018).
- ⁴⁸A. Roshko and G. J. Thomke, "Observations of turbulent reattachment behind an axisymmetric downstream-facing step in supersonic flow," *AIAA J.* **4**, 975–980 (1966).
- ⁴⁹H. Liu, B. Wang, Y. Guo, H. Zhang, and W. Lin, "Effects of inflow Mach number and step height on supersonic flows over a backward-facing step," *Adv. Mech. Eng.* **5**, 147916 (2013).
- ⁵⁰I. Bolgar, S. Scharnowski, and C. J. Kähler, "The effect of the Mach number on a turbulent backward-facing step flow," *Flow, Turbul. Combust.* **101**, 653–680 (2018).
- ⁵¹Z. Chen, S. Yi, L. He, L. Tian, and Y. Zhu, "An experimental study on fine structures of supersonic laminar/turbulent flow over a backward-facing step based on NPLS," *Chin. Sci. Bull.* **57**, 584–590 (2012).
- ⁵²J. Jeong and F. Hussain, "On the identification of a vortex," *J. Fluid Mech.* **285**, 69–94 (1995).
- ⁵³M. Chang, X. Meng, Z. Fu, and J. Bai, "Study on flow characteristics of compressible laminar flow boundary layers," in *Proceedings of the 2018 Asia-Pacific International Symposium On Aerospace Technology* (Springer, 2019), pp. 451–463.
- ⁵⁴W. Eissler and H. Bestek, "Spatial numerical simulations of linear and weakly nonlinear wave instabilities in supersonic boundary layers," *Theor. Comput. Fluid Dyn.* **8**, 219–235 (1996).
- ⁵⁵Y. Ma and X. Zhong, "Receptivity of a supersonic boundary layer over a flat plate. Part 3. Effects of different types of free-stream disturbances," *J. Fluid Mech.* **532**, 63–109 (2005).
- ⁵⁶T. Hiejima, "Streamwise vortex breakdown in supersonic flows," *Phys. Fluids* **29**, 054102 (2017).
- ⁵⁷J. Z. Wu, H. Y. Ma, and M. D. Zhou, *Vorticity and Vortex Dynamics* (Springer, Berlin, Heidelberg, 2006), pp. 1–776.
- ⁵⁸S. Suryanarayanan, D. B. Goldstein, and G. L. Brown, "Roughness induced transition: A vorticity point of view," *Phys. Fluids* **31**, 024101 (2019).
- ⁵⁹T. Michelis, S. Yarusevych, and M. Kotsonis, "On the origin of spanwise vortex deformations in laminar separation bubbles," *J. Fluid Mech.* **841**, 81–108 (2018).
- ⁶⁰O. Marquet, D. Sipp, J.-M. Chomaz, and L. Jacquin, "Amplifier and resonator dynamics of a low-Reynolds-number recirculation bubble in a global framework," *J. Fluid Mech.* **605**, 429–443 (2008).
- ⁶¹C. Cerretelli and C. H. K. Williamson, "The physical mechanism for vortex merging," *J. Fluid Mech.* **475**, 41–77 (2003).
- ⁶²T. Leweke, S. Le Dizès, and C. H. K. Williamson, "Dynamics and instabilities of vortex pairs," *Annu. Rev. Fluid Mech.* **48**, 507–541 (2016).
- ⁶³A. Sansica, N. D. Sandham, and Z. Hu, "Instability and low-frequency unsteadiness in a shock-induced laminar separation bubble," *J. Fluid Mech.* **798**, 5–26 (2016).
- ⁶⁴C. R. Smith and S. P. Metzler, "The characteristics of low-speed streaks in the near-wall region of a turbulent boundary layer," *J. Fluid Mech.* **129**, 27–54 (1983).